PETROPHYSICAL CHARACTERIZATION OF GAS RESERVOIR ROCK SAMPLES USING HIGH RESOLUTION MICRO-CT IMAGES

By Georgios Krassakopoulos

Delft University of Technology

Aknowledgements

This thesis would not have come to completion without the invaluable assistance of many people.

First I would like to address special thanks to my thesis supervisors, Professor Dr. Pacelli L. J. Zitha and Christian Kosack:

Professor Zitha for his patience, support and motivation towards improving my technical writing. Christian for his invaluable assistance in every stage of this thesis and for taking the time off his own research to help me.

Additionally I would like to thank the members of my examination committee for reading and approving my MSc thesis.

From the laboratory staff I would like to thank Dick for the assistance in extracting micro-plugs, milling plug surfaces and for other relevant torture we subjected the original samples to. Wim for invaluable assistance during the Micro-CT scanning and pre-processing phase. Karel for providing the experimental set-up and assisting in the analog measurements of porosity. Helen and Joost for allowing me use of the high-specification hardware with which I ran part of my permeability simulations.

Professor Dr. Karl-Heinz Wolf for allowing me access to the laboratory, providing me with useful input at times and for his patience during my long presence in the lab during the summer.

Assistant Professor Auke Barnhoorn for sharing his experience with image processing, particularly on feature extraction.

Menno Bloemsma for his assistance in contacting PanTerra GeoConsultants BV and mediating for me to run my micro-permeameter tests there.

From PanTerra GeoConsultants BV I would like to thank mr. Mike Burns, Madhavi Patandin, Lida Maria Soukouli and all the technical personnel for facilitating me during my time in their core lab. Additionally, Dr. Jos Maas for the very insightful talk we had during our meeting in TUDelft.

All of the PhD students for bearing with my presence in their ‘sanctuary’ on the ground floor.

I would like to thank my parents for the financial and moral support during my studies and my friends for always being there.

Abstract

Petrophysical analysis of reservoir rocks constitutes an integral part of hydrocarbon exploration and production. Properties such as porosity and permeability greatly influence decision making in all phases of planning and execution of oil and gas activities. Furthermore, the industry and academia are equally interested in the in-depth investigation of pore network properties of porous rock in order to advance studies on flow and solid-fluid phase interaction.

Typically, petrophysical analysis is conducted through 'analog' testing of rock samples using equipment that derive the aforementioned properties through direct physical interaction. Such methods share limitations derived from a non-integrated, non-standardized overall methodology, manifesting as variable error of measurements.

The present thesis proposes a digital image based petrophysical analysis method that aims to mitigate such limitations through detailed monitoring. Through the application of an integrated scan-to-measurements process, 3D X-Ray images of five core plugs originating from a Dutch gas offshore field are thoroughly analyzed. Petrophysical properties such as porosity and permeability are quantified, but the methodology also assesses and quantifies pore network features such as grains, pores and pore throats. All steps of this process are thoroughly described, along with - where applicable - alternate relevant approaches.

The results of this image based petrophysical analysis are compared to measurements obtained through the use of conventional core analysis methods, as well as relevant literature. The outcome of this comparison illustrates the strengths and areas of improvement of the proposed methodology. Conclusively, the reasoning for transitioning from 'analog' to image based petrophysical analysis is validated, and a future outlook is also presented.

Table of Contents

List of Figures

List of Tables

List of Equations

1. INTRODUCTION

In the near future, projected energy demand is expected to rise. The energy mix still favors fossil fuel and as such this translated to increased demand for hydrocarbons. With oil and gas production from conventional reservoirs continuously declining, unconventional reservoirs (tight gas, shale gas, coalbed methane) become increasingly relevant. The characterization of such types of reservoir is significantly harder than that of conventional reservoirs. This is due to their highly complex pore network and the difficulties imposed on the application of conventional methods of petrophysical analysis.

Petrophysical analysis of rock samples traditionally uses techniques that focus on the determination of a single property at a time. The petrophysical properties that characterize the rock layers of which oil and gas reservoirs consist determine volumes of hydrocarbons, drilling plans and production/injection methods alike. Porosity directly influences Hydrocarbons Initially in Place (HIIP) or reservoir storage capacity calculations. Permeability (absolute and relative) determines the evolution of a producing/injected reservoir through assessing its capacity to transmit fluids in the micro and macro scale. Lithology determines the boundary between reservoir and non-reservoir as well as addressing other issues such as salt precipitation in production lines. Fluid saturation also directly affects the estimation of resources at play as well as underlining localized challenges related to potential phase override (water-cut, gas coning, erratic flow regimes etc).

Petrophysical properties are typically measured by well logging (for large scale measurements) and laboratory analysis (for small scale analysis).

Well logs are acquired through the use of geophysical tools moved along the borehole of drilled wells either attached to the drill string (logging while drilling - LWD) or through the use of wireline. They measure gamma ray response, caliper, density, neutron porosity, resistivity, and acoustic impedance (sonic). Measurements from well logs are subsequently combined with sample based results in order to fully characterize the reservoir.

Sample analysis is conducted in specialized laboratories. In order to determine the petrophysical properties of (typically) either full cores or core plugs, a wide array of destructive and non-destructive tests are conducted, where standardized equipment such as porosimeters and permeameters are used. Despite advances in conventional methods of petrophysical analysis, the results often carry elements of uncertainty in measurements.

The present thesis attempts to establish the background of an integrated scan-to-measurements petrophysical analysis method based on the use of 3D μCT images. Conventional core analysis methods are also applied in order to evaluate the validity of those results.

The theoretical background of the thesis is established in chapter 2, followed by the description of the proposed methodology in chapter 3. The results are presented in chapter 4 along with observations on the process. In the conclusive part of the thesis (chapter 5) the overall outcome of the thesis is evaluated, and the relevant future research outlook is also discussed.

2. BACKGROUND

In this chapter, the theoretical background to the development of the methodology is presented.

2.1 μCT Imaging

Originally developed for medical use in the early 70s, Computerized Tomography (CT) has since provided a non-destructive method for investigating the internal structure of both animate and inanimate objects.

CT scanning is based on the principle of density contrasts (and void space) within an object. This density contrast results in differential attenuation of X-Rays travelling through that object. Captured through a detector, these attenuations translate to a grayscale 3D image of that object, composed of voxels. Each voxel has a different grayscale value corresponding its density. Denser materials correspond to grayscale values of a lighter intensity, closer to white. Void and saturating fluids typically assume darker values, closer to black. This 3D image can be subsequently exported to other specialty applications where it is possible to further process it in order to make qualitative and quantitative observations on the internal structure of the imaged sample.

The adoption of CT scanning by material sciences led to the development of a variant, capable of imaging resolution of as low as 2 microns, aptly named μCT. μCT scanning can be used to image the internal structure of sedimentary rock samples, owing to the density contrast amongst constituent grains, as well as between the matrix as a whole and void space.

Significant advances in three dimensional imaging due to an enormous increase of computational capabilities in the beginning of the century have resulted in a significant amount of petrophysical research projects that utilize μCT images (Al-Kharusi, 2006; Arns, 2004; Cnudde, 2005; Degruyter, 2005-2006; Dong, 2007; Saites, 2006; Dullien, 1992; Fens T. W., 2000; Mostaghimi, 2012; Al-Raoush, 2005) as well as (Youssef, 2008; Akin, 2003; Shin, 2002; Siddiqui, 2009). The Society of Core Analysts (SCA) has also embraced μCT image analysis as part of the modern toolset of core analysis.

Most of the volume of such research (including the aforementioned citations) is targeted towards either the in depth investigation of sample properties, utilizing custom approaches to do so, or on the improvement of image analysis process 'components' (Al-Ansi, 2013).

Image based core analysis in 2D is present in literature (Prince, 2002; Fens T. J., 1991; Fens T. W., 2000), where the importance of digital image analysis of core imagery has been identified as having the potential to increase the amount of information that can be extracted from cores. The aforementioned papers define the starting point of this thesis. Elements from the recent relevant research of S. Zhang et al. (Zhang, 2011) are also taken into consideration.

2.2 Thesis Outline - Description of Methodology

The outline of this thesis is presented in Figure 1 as a flowchart.

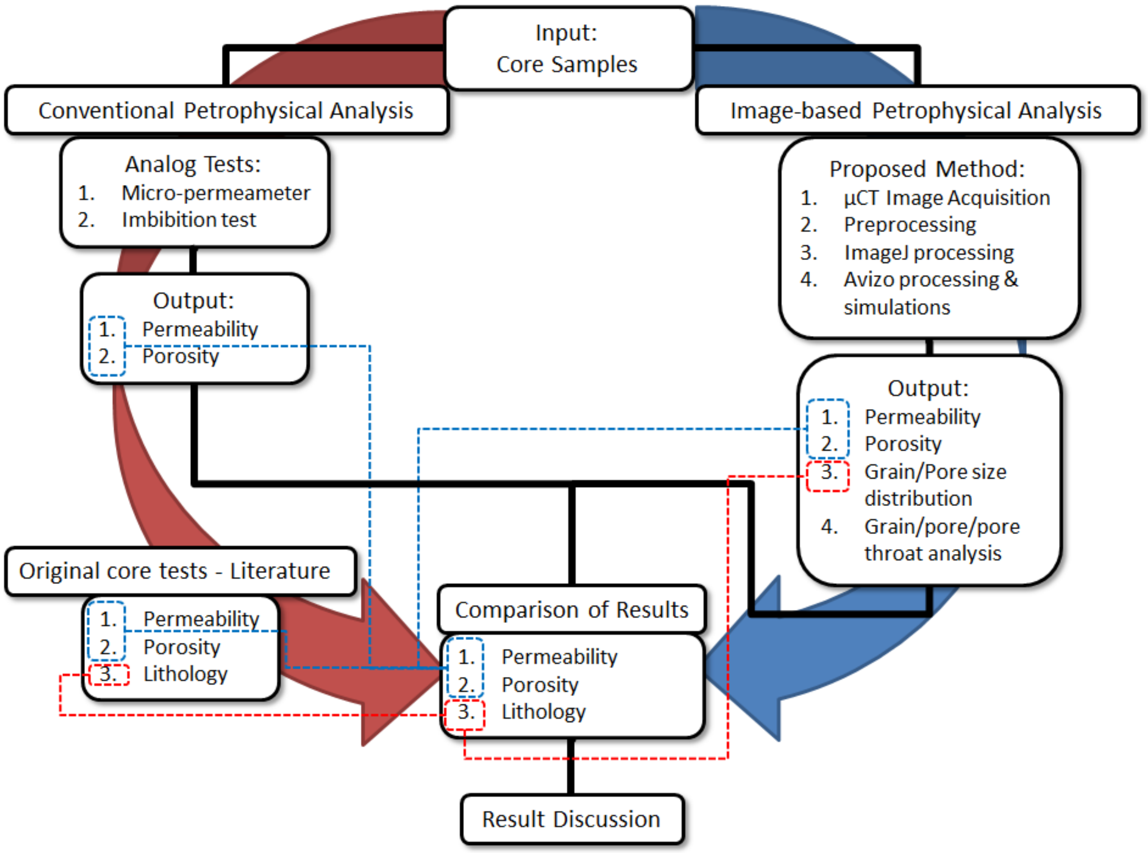

Figure 1: Methodology Flowchart

The top part of the visualized workflow (input) includes all tasks relevant to the preparation of the core samples for the needs of the various experiments (chapter 2.3). The right side (blue arrow) describes the four steps to the methodology that account for the major bulk of this thesis (chapter 3.1). The left side (red arrow) represents conventional petrophysical analysis measurements taken from the cores (chapter 3.2). Along with historical data from the original core run and relevant literature (chapter 2.3, Appendix), these 'analog' petrophysical analysis methods make up the qualitative control part of the proposed methodology. The bottom part of the flowchart illustrates how the output of the two analyses are compared (chapter 4). Dotted lines indicate compared properties. Permeability and porosity output from the image based method is compared to the measurements from the respective analog methods, as well as historical data. Grain and pore size distributions are compared to relevant literature in order to assess the lithology of the originating formation.

2.3 Core Samples - Preparation

Five core plugs were used as samples in this thesis. The cores originate from the Dutch offshore gas field P18-2. The well they originate from is called P18-A-01 (see Figure 2) and was drilled in 1990 for Amoco as an appraisal well. The well is a currently producing gas well. Source: (NL Oil and Gas Portal).

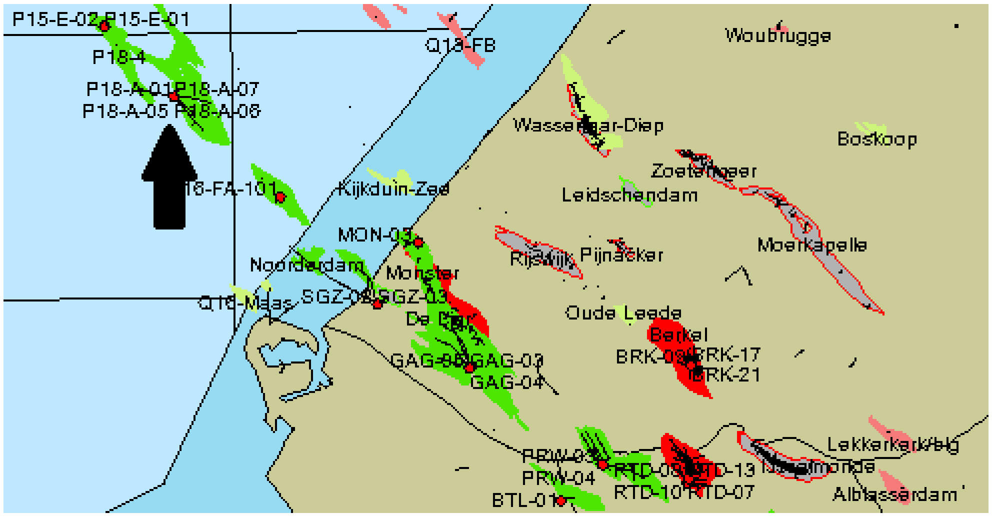

Figure 2: Location of Originating Field and Well; Source: (NL Oil and Gas Portal)

The naming convention used over this thesis for the five samples is CK1 through 5. All plugs originate from the Hardegsen Formation (NL Oil and Gas Portal). The formation is defined as: '*Uptriasost cycle of the Main Buntsandstein, comprising several stacked alternations of off-white to pink sandstones and red claystones. The regular alternation of these lithologies is typical for the member. In the southern Netherlands onshore and offshore the member is predominantly composed of arkosic sandstones without claystone intercalations*' (DINOloket - Data en Informatie van de Nederlandse Ondergrond). Based on the results of the original core analysis, the first three plugs originate from the same reservoir formation (sandstone), while the other two come from the stratigraphic formation directly under the reservoir (claystone or shale). The following table (Table 1) denotes their respective originating TVD (true vertical depth) interval, while pictures of all the core plugs can be found in the Appendix.

Table 1: Originating depth of Core Plug Samples

Core plug	TVD(m)
CK1	3627-3628
CK2	3638-3639
CK3	3640-3643
CK4	3649-3650
CK5	3650-3651

Each of the core plugs is 4cm in diameter and roughly 3cm long (see Figure 3) in their initial state. The cores were prepared in various ways according to the requirements of the µCT scanning phase and the conventional tests. The reasoning behind each of these preparatory processes is expanded upon in chapter 3, in the description of the individual tests.

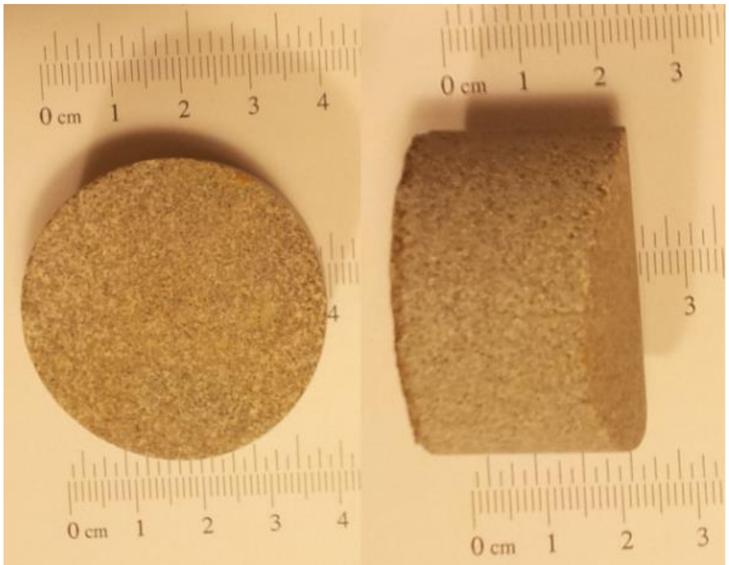

Figure 3: Sample Original Plug

In their original state, the cores were used in the first round of µCT scanning. They were also used in the first round of micro-permeameter measurements. After that, 'micro-plugs' of 8mm in diameter (see Figure 4) were extracted from the original plugs using a special diamond tip drill, in order to improve the accuracy of the µCT scans. The same micro-plugs were also used in the imbibition test for the conventional determination of porosity.

Figure 4: Sample Extracted Micro-plug and Original Plug 'Shell'

Finally, the remaining 'shells' of the original cores (Figure 4) were used in the second round of the conventional determination of permeability through the micro-permeameter. However, another modification was conducted on them, where a flat surface was flattened along their main length as seen in Figure 5, in order to facilitate micro-permeameter usage on them along that axis.

Figure 5: Flattened Surface on Original Plug 'Shell'

2.4 Image Processing Tools

Image processing refers to a process in which both the input and the output are images. One of the most relevant processes typically accomplished through the use of digital image processing is feature extraction, which is important in the present research. Feature extraction corresponds to the application of algorithms that detect and isolate select portions of the processed images. This is the process that defines the difference between pore space and the solid matrix. Additional image processing features are employed towards specific tasks, mostly towards improving image quality and thus facilitating feature extraction, but also to perform other tasks, such as feature segmentation, logical operations and filtering. The reconstruction of μCT 3D output to stacks of images and the filtering applied by the μCT software during acquisition (as seen in 3.1.1) also constitutes image processing. The image processing operations used in this research are explained in more detail in chapter 3.1.2 and 3.1.3.

Image analysis typically follows image processing, with (processed) images constituting the input once again, while the output is a set of measurements in an exportable format. Image analysis also relates to a limited degree of dynamic modeling which simulates experiments, as will be seen in the measurement of permeability in 3.1.3.

The software used in the processing and analysis of the core sample images was selected with the following criteria in mind:

Based on the criteria such as range of processing options, monitoring of processes and access to a developer community and/or support, two individual software suites were identified as appropriate for the processing and analysis of the image stacks:

1. **ImageJ** is a public domain Java-based image processing and analysis program. It runs, either as an online applet or as a downloadable application, on any computer with a Java 1.5 or later virtual machine. It can display, edit, analyze, process, save and print 8–bit, 16–bit and 32–bit images as well as accept multiple image formats as input, including TIFF, GIF, JPEG, BMP, DICOM, FITS and ‘raw’. It also supports importation of image stacks as a single input. It is a multithreaded application, which means it takes

advantage of multi-core processor architecture in order to run multiple processes at the same time, something important in the processing and analysis of image stacks as regards time-efficiency.

One important feature of ImageJ is that, apart from the basic suite of processes which covers most of the standardized processing and analysis operations, it allows for inclusion of custom scripts towards either automating existing processes or adding new ones. A very active multidisciplinary community continuously adds and updates publicly available content.

In the present research, ImageJ was used in further filtering and processing of the μCT images, as well as in determining the total porosity of each of the image stacks – samples through custom scripts.

2. **Avizo**, from FEI Visualization Sciences Group, is a general purpose 3D image visualization, analysis and modeling software application. While not open source like ImageJ, it does come in various editions tailored to specific application areas such as materials science - industrial inspection, simulation data, geosciences - oil & gas, environment & climate, and other optional modules. The main advantages of Avizo are:
    a. It is software specifically designed and maintained towards the processing and analysis of 3D data, thus offering very good special (though not custom) features.
    b. It has a very interactive visual user interface which helps visualize and optimize processes.
    c. An optional computation package for permeability is readily available for Avizo.

   It is not however, exclusively used in this research because of some of its disadvantages:
    a. As a commercial application, detailed information is not provided in the implementation of certain operations, something crucial to sensitivity analysis and further theoretical improvement of the method.
    b. It lacks the customizability offered by open source platforms such as ImageJ.

   Avizo was used for advanced image segmentation processes, as well as for the modeling and determination of permeability in the image stacks – samples and for feature extraction.

2.5 Analog Testing

A set of conventional core analysis tests was carried out on the plugs, in order to impose a degree of qualitative control, by comparing the results from the image analysis of the cores to results from established methods so as to assess the accuracy of the μCT measurements and processing methods.

The tests that were conducted are:

- Permeability measurements using a probe (mini-) permeameter.
- Porosity measurements using an experimental setup based on measuring volume, wet and dry mass.

The details of those experiments will be expanded upon in 3.2.1 and 3.2.2 respectively, along with the equipment involved in each test.

3. METHODOLOGY

In this chapter, the proposed methodology will be laid out in detail (3.1), followed by a description of the conventional core analysis ran alongside the method (3.2)

3.1 μCT Imaging and Analysis

The steps to the proposed methodology are presented in sequence below.

3.1.1 μCT Image Acquisition

The principle of operation of the μCT scanner is the acquisition of 360^o radioscopic image representation (see chapter 2.1) of the inspected object.

The set up required for such a scan consists of a micro focus X-Ray tube for projection opposite an X-Ray image intensifier and camera, with a rotating sample table in between them. The object is placed on the sample table and multiple 2D X-Ray images (up to 2400 slices in a single rotation) are obtained using the X-ray image intensifier by turning and/or vertically shifting the table while irradiating the object with X-rays.

The imaging system set-up in μCT scans usually follows one of the following configurations:

- Fan Beam: Fan beam system consists of a one-dimensional X-ray detector and an electronic X-ray source, which creates 2D cross-sections of the object through the rotation of the turntable on which the sample is placed. Complete vertical slices are assembled through the vertical shifting of the turntable along its Z axis between rotations.
- Cone beam: The cone-beam system consists of a 2D (planar) X-ray detector (camera) and an electronic X-ray source. It automatically captures a full vertical slice during every rotation.

In either configuration, the distance between the source and the detector determines the resolution of the acquired images. Both of the set-ups can be visualized in Figure 6.

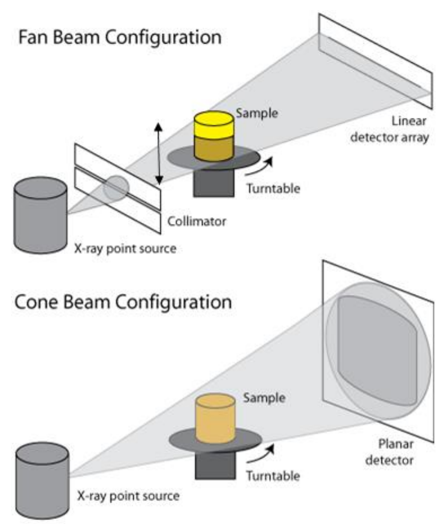

Figure 6: μCT Scanner Imaging System Configurations (The Science Education Resource Center at Carlton College, 2013)

A 'phoenix nanotom S' μCT scanner (see Appendix) was used for the extraction of a 3D image dataset from the core plugs. The cone beam set-up was used, as it was considered preferable to retrieve full vertical slices rather than reconstructed vertical slices, which reduces subsequent reconstruction-related error to only the lateral direction. Additionally, the combination of continuous vertical and rotational movement increases the risk of minute alterations on the absolute position of the sample, which usually results in imaging errors (optical artifacts).

Two series of scans were conducted, initially on the core plugs and subsequently on the extracted micro-plugs. The common parameters for both series of acquisitions are presented below:

- X-Ray Voltage: 110kV
- X-Ray Amperage: 130µA *(The amperage in the X-Ray settings affects the gray values in the acquired images and was optimized with that in mind.)*
- 1440 images acquired per plug (0.25 degrees of rotation between each image)
- Timing of 500msec
- Averaging over 5 images
- Skipping of 2 frames

The cylindrical micro plug imaged volumes are exported from the µCT in the format of '.Tiff' 16-bit grayscale image stacks. Each image in the stack is a circular grayscale slice of the cylinder and represents 1 voxel in the third dimension (perpendicular to the plane defined by the image).

In the first scanning roung 4cm diameter plug images were acquired at a resolution of 40 microns (40µm voxel size). The imaging quality was too low to determine the internal structure of the imaged samples and make quantitative measurements in latter stages of the methodology, therefore a second round of scans was conducted using the 8mm diameter mini-plugs. Due to the decreased distance between source and detector, as well as due to the narrower focus of the beam (from 4cm to 8mm), a more detailed resolution of 2.5 microns (2.5µm voxel size) was achieved. The resulting improvement in the differentiation of the grayscale range can be seen comparatively in the following Figure 7.

The disadvantage of the high resolution images (2.5µm) is that, due to the increased resolution, imaging the entire microplug represents a tremendously large amount of data (>100 Gigabytes per core). Thus, a only part of the microplug (2.5mm long cylinder) is extracted as data for further processing.

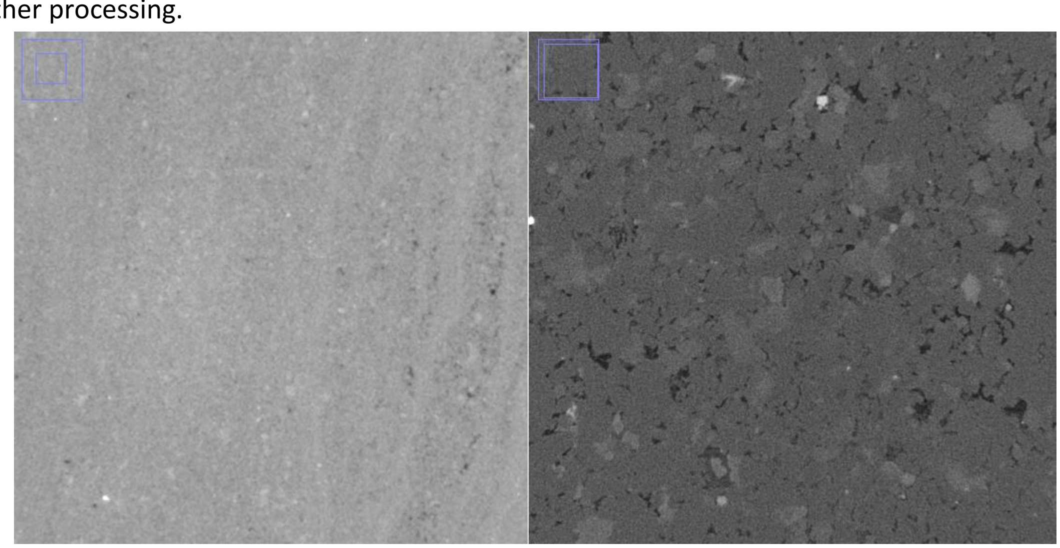

Figure 7: Comparison of Different Resolution Images of the Same Core (Left - 40µm, Right - 2.5µm)

Some visual artifacts were also created during the scanning phase. Their types and causes are described below:

- Beam hardening artifacts: caused by high attenuation objects.
- Ring artifacts: caused by a combination of a miscalibrated detector and miscalibrated rotating sample. They were only encountered in the high resolution (2.5µm) images,

where precise calibration was not possible and slight tilting of the vertical axis was magnified.

- Shading artifacts: manifesting around large patches of high density minerals as dark streaks. Similarly to ring artifacts, they were also only discernible in the high resolution images.
- 'Halo' artifacts: streaks of luminosity surrounding the outer rim of the round image slices. Only discernible in the higher resolution images. They are the result of varying intensity of X-rays travelling through the sample

A series of preprocessing and filtering operations were conducted using the µCT setup software (datos|x CT) in order to eliminate or reduce the effects of most of the aforementioned visual artifacts.

- Beam hardening was directly addressed by the acquisition software during the image reconstruction, by applying a built in beam hardening reduction algorithm at a setting of 9.85 out of 10.
- Shading artifacts are only prominent in localized large mineral patches. The image reconstruction area was chosen to exclude such patches, since the shading effect assumes the same grayscale hues like pore space and no reliable algorithm was available to mitigate this.
- Ring artifacts are only prominent in a very small area around the axis or rotation. They occupy a very limited range of grayscale values and as such can be eliminated during further image processing or their presence does not affect subsequent processing.

A filtering process was applied in order to clean up the images from small scale noise. A median grayscale value was chosen between 3 voxels in each direction as long as their values are closely matched.

3.1.2 ImageJ Processing & Analysis – Determination of Porosity

As discussed previously, µCT imaging on the core micro plugs yielded five grayscale image stacks which describe the preprocessed 3D volumes at a resolution of 2.5µm. Each of the images in the stack is approximately 2140 pixels (image volume=voxels, single image=pixels) in diameter (see Figure 8).

In order to determine the porosity and permeability of the imaged samples, it is first important to establish the boundary between the solid matrix and pore space. In grayscale images this is possible through the application of a segmentation process.

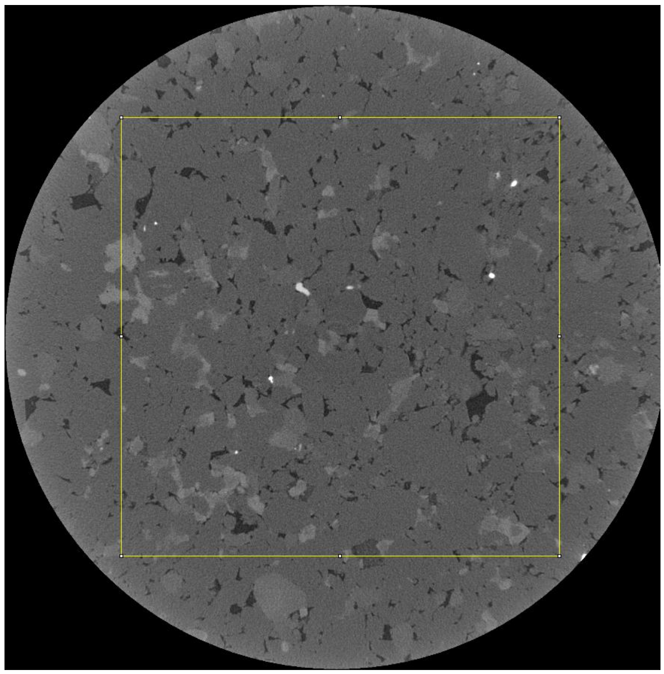

Figure 8: Sample µCT Output Slice and Cropped Area (within Yellow Border)

Prior to segmentation it is important to crop the image stacks from a cylindrical shape to a rectangular parallelepiped shape. Practically, this means cropping each slice to a square (Figure 8). Cropping the images is an essential step despite the loss of some of the imaged volume:

1. A rectangular parallelepiped shape is easier to manage and process using 3D image processing software due to the layout of the visual interface, which facilitates processing of rectangular parallelogram shaped slices.
2. A coordinate system is easier to apply on such a shape, which is crucial during permeability vector estimation and feature mapping later on.
3. It removes the effects of near edge artifacts such as the halo artifact discussed in 3.1.2.

The resulting volume of each of the imaged samples is presented below, in Table 2. For the rest of this paper this is the volume of reference for the sample as regards image processing and analysis.

Table 2: Imaged Dimensions and Volume of the Core Samples

Sample	Total Dimensions (pixels)	Total Dimensions (μm)	Total volume (mm^3)
CK1	1410 X 1410 X 995	3522.5 X 3522.5 X 2487.5	30.865
CK2	1410 X 1410 X 994	3522.5 X 3522.5 X 2485	30.834
CK3	1410 X 1410 X 989	3522.5 X 3522.5 X 2472.5	30.679
CK4	1410 X 1410 X 991	3522.5 X 3522.5 X 2477.5	30.741
CK5	1410 X 1410 X 988	3522.5 X 3522.5 X 2470	30.648

The required segmentation result for this research is the distinction of the pixels present in every image to two classes. The segmentation algorithm allocates the constituent pixels on each image slice to either one of two pixel groups (segments) that represent the two aforementioned classifications (matrix – void).

In the grayscale image stacks, information is stored in a 16-bit format (65000 shades of grey), where the grayscale value of each pixel corresponds to imaged density. Through binarization, each pixel is instead assigned one of two values, which, varying throughout literature, are defined as 0 and 1, white and black, or foreground and background. The two values represent pore space and solid matrix respectively. Furthermore, turning the image into a binary form gives access to a large toolset of (further) segmentation, logical operation and quantification algorithms directly embedded in the architecture of image processing software.

There are various methods used to segment images, such as edge detection, clustering methods, compression methods, region growing methods, histogram methods and thresholding methods.

Grayscale images are predominantly segmented into binary form through thresholding. In literature (Sankur, 2004), the available thresholding methods are categorized into the following six groups based on the type of manipulation of information conducted by the algorithm:

- Histogram shape-based methods: the peaks and valleys of the derived grayscale histogram are analyzed.
- Clustering-based methods: the gray-level samples are grouped in two parts as background and foreground.
- Entropy-based methods: algorithms that use the entropy of the foreground and background regions, the cross-entropy between the original and binarized image.
- Object Attribute-based methods: algorithms that look for a measure of similarity between the gray-level and the binarized images, such as fuzzy shape similarity, edge coincidence, etc.
- Spatial methods: algorithms that use high-order probability distribution and/or correlation between pixels
- Local methods: algorithms that adapt the threshold value on each pixel to the local image characteristics.

Thresholding options in ImageJ include various established methods. It is important to select an adequate threshold of gray level for extracting objects from their background. To do that, it is important to choose an appropriate algorithm from the aforementioned list. In an ideal case, a histogram based method is utilized, where the histogram has a deep and sharp valley between

two peaks representing objects and background, respectively, so that the threshold can be chosen at the bottom of this valley.
In our case, as is true for most μCT scans, such a distinction between peaks either does not exist, or is not representative of the actual threshold and needs to be manually adjusted (see Figure 9).

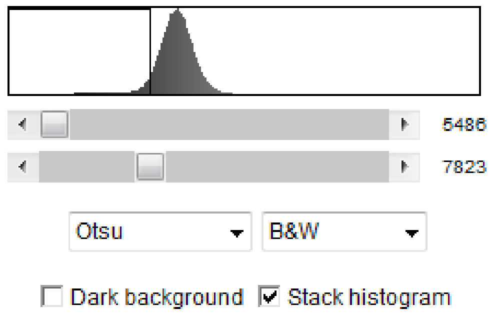

Figure 9: Sample Grayscale Value Histogram for one of the Imaged Volumes

In such a scenario the most applicable automated method proposed in literature is Otsu's method (Otsu, 1979). The algorithm operates under the assumption that the image to be thresholded contains two classes of pixels or a bi-modal histogram (for example foreground-background). Subsequently it exhaustively searches for the threshold that minimizes intra-class variance.
Through various trials, it was indeed verified that Otsu's method is the best available compromise between an automated algorithm and a quality result. Thresholding uses the stack of images as reference (see Figure 9, 'Stack Histogram' checkbox) rather than individual slices, in order to account for local variations in local grayscale luminosity, something that was largely mitigated through cropping of the 'halo' artifact, but not entirely eliminated.
The output of this operation is a series of binary images. What followed was the application of a series of logical binary operations in order to improve the quality of the binarized output. The two main quality diluents at this stage are:

- Despite the smoothing filtering applied during pre-processing of the grayscale images, some pixels attributable to matrix volume have instead been classified as pore space by the thresholding algorithm. This manifests as isolated 'pore' pixel clusters (1-9 voxels large) within matrix space.
- Inversely, some small to medium size pixel clusters within large pores have assumed matrix classification.

In order to address these commonly occurring visual artifacts, two types of operations are performed:
Hole fill: The hole filling algorithm performs the namesake function of altering the binary value of pixels from one class fully enclosed by the other class to match that of the surrounding pixels (see Figure 10). This operation corresponds to the elimination of matrix pixels within the pores.

Figure 10: Example of the Hole Filling Algorithm in 2D

Open: Morphological opening is defined as an erosion cycle followed by a dilation cycle. In binary images, erosion effectively corresponds to the removal of a 'layer' of pixels from the perimeter of the specified class. Dilation is the inverse process that adds an extra 'layer' of pixels on the outer perimeter of each object of the specified phase. The combined effect of opening effectively removes small objects from the specified phase. The affected larger pores return to their original state more or less, with the exception of some very small features such as the protrusions seen in Figure 11, which are eliminated.

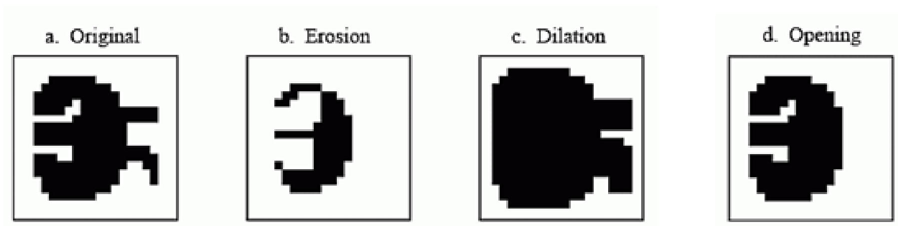

Figure 11: Example of the Opening Algorithm with Intermediate Steps in 2D (Smith, 2013)

These morphological processes are typically conducted in a 2D environment, namely on single images. Since the scope of this thesis deals with 3D volumes, however, an upscaled version of these processes was chosen that performs these operations in 3D.

For these 3D operations Fiji (Schindelin, 2012), a special ImageJ processing package was used. Its extensive list of 3D features, originally developed for the analysis of biological images, is applicable to the requirements of this research.

The result of this process can be seen in Figure 12, where an initial grayscale slice is presented alongside the processed binarized output.

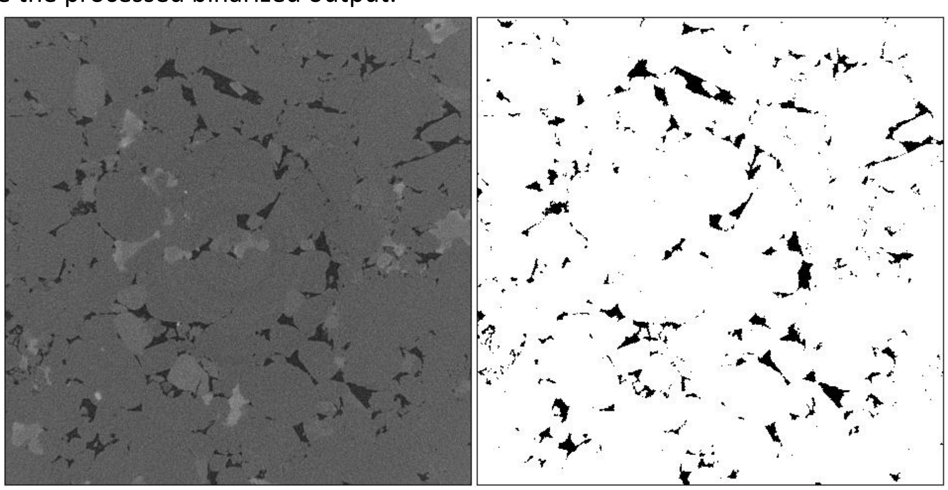

Figure 12: Comparison between Grayscale (left) and Binarized (right) Image Slice

Porosity is a measure of the ratio of pore volume over the total volume of a sample. For the determination of porosity from the now defined pore space, another ImageJ plugin was utilized, BoneJ (Doube M, 2010). BoneJ is another plugin developed for the medical industry, to cater to processing and analysis of bones. It has been successfully used in the analysis of µCT scans of cancellous bone (Hildebrand, 1999), which shares many similarities with porous rock. BoneJ is able to calculate volume fractions from binary image stacks using two algorithms:

- Voxel Counting: Explicit method that accounts for all voxels attributed to the pore space phase.
- Surface mesh: Using a marching cubes algorithm (Lorensen, 1987) a 3D surface is constructed within the pore voxels using triangular models. Subsequently, the enclosed volume is accounted for (see Figure 13). This algorithm has the advantage of approximating pore morphology more accurately than stacked voxels. However it also dismisses parts of potentially attributable porosity and so its end result is a measurement of porosity lower than the voxel counting method.

Both methods were used towards the determination of porosity. The results can be found in 4.1.1.

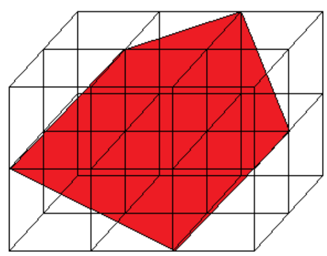

Figure 13: Surface Mesh Algorithm: Accounted Volume (red) and Originating Voxels (grid)

3.1.3 Avizo-Permeability-Feature Extraction

The determination of permeability from an image based dataset represents an arguably more difficult task than the determination of porosity. This is due to the fact that the connection between the physical property and information directly attainable from a μCT scan is not explicit. In order to establish a relationship between the product of the scans and permeability estimation, a computational method is required to be incorporated in the processing algorithm.

While not within its core capabilities, ImageJ is potentially capable of such computational analysis through the implementation of scripting and plug-ins. However, the development of such a computational plug-in is not within the scope of this research. Therefore, further processing and analysis on the imaged dataset was conducted using the Avizo software suite described in 2.4.

Avizo uses the binarized format of the imaged volume described in 3.1.2 as input for the permeability computations. The XLab Hydro computational module is capable of numerically estimating absolute permeability through simulation of a flow experimental setup.

The simulated experiment generates a constant disequilibrium between two opposite faces of the sample. The other faces are hermetically closed. In this experimental setup, simulated fluid 'runs' through voxels defined as pore space in the binarized volume. For each of the X, Y and Z directions, a single axis flow path is created as depicted in Figure 14.

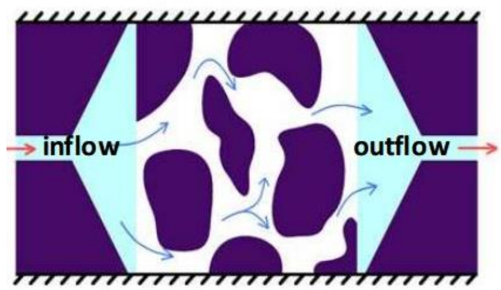

Figure 14: Example of Avizo Simulated Flow Experiment in 2D (Zhang, 2011)

Boundaries are placed the outer planes of the image volumes except the ones defined as inflow-outflow. Simulated fluid flow first enters a divergence inflow channel before it enters the imaged porous structure. Similarly, during outflow, it first enters a convergence channel before it is released. The inflow and outflow zone are added to accommodate the complex porous shape of the sample faces where the fluid goes in and out, to increase numerical stability (Zhang, 2011). A visualization of the actual modeled flow can be seen in Image 15, where the rendered flowlines can be seen converging in the inflow and outflow areas.

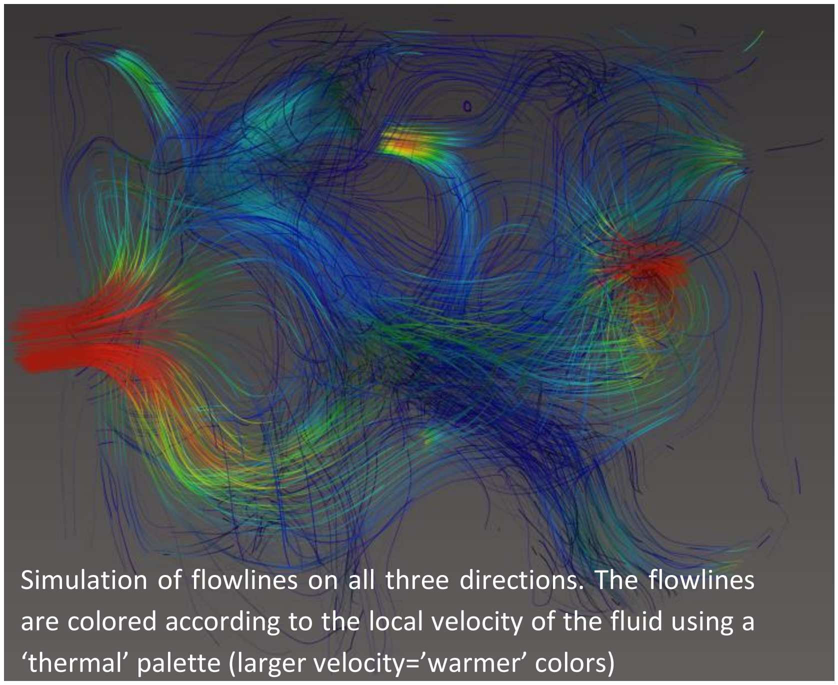

Figure 15: Simulated Flowlines in 3D

The theoretical foundation of this simulation is the 3D expression of the following Stokes equation system (Stokes., 1845):

Equation 1: Stokes Equation System (Stokes., 1845)

$$\begin{cases} \vec{\nabla} \cdot \vec{V} = 0 \\ \mu \nabla^2 \vec{V} - \vec{\nabla} P = \vec{0} \end{cases}$$

Where:

- $\vec{\nabla} \cdot$ is the divergence operator
- $\vec{\nabla}$ is the gradient operator
- $\vec{V}$ is the velocity of the fluid in the fluid phase of the material
- μ is the dynamic viscosity of the flowing fluid
- ∇^2 is the laplacian operator
- P is the pressure of the fluid phase of the material

In order to numerically approximate this analytical system, a finite volume method is applied by the solver (VSG, 1999-2013). The equations are discretized in a staggered grid arrangement, where the isotropic (cubic) voxels represent grid cells. Pressures unknowns are located at the center of the voxel while velocity unknowns are decomposed at the faces of the voxels (see Figure 16). An artificial compressibility scheme is employed to solve pressure (at the center of the grid) and velocity (at the boundary of the grid).

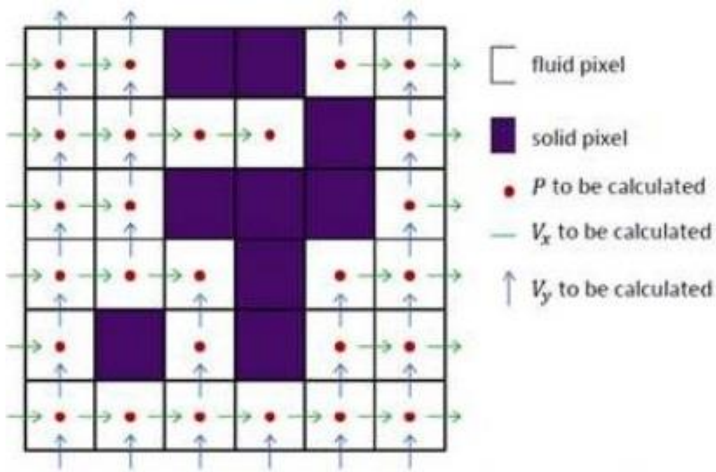

Figure 16: 2D Visualization of the Discretized Grid Showing the Location of System Unknown Values (Zhang, 2011)

The set of boundary conditions present in this solution are described as follows:

- No-slip condition at fluid-solid interfaces.
- A one-voxel-wide plane of solid phase (with no-slip condition) is added on the faces of the image that are not perpendicular to the main flow direction. This allows isolation of the sample from the outside, allowing no flow out of the system.
- Experimental setups are added on the faces of the image that are perpendicular to the main flow direction. They are designed in a manner that creates a stabilization zone where pressure is quasi static, and the fluid can freely spread on the input face of the sample.
- Two among the following three conditions can be chosen by the user, the third being estimated from the chosen two: input pressure, output pressure, flow rate.

Once the equation system has been solved, permeability is calculated through the application of Darcy's Law (Darcy, 1856):

Equation 2: Darcy's Law (Darcy, 1856)

$$\frac{Q}{S} = \frac{k\Delta P}{\mu L}$$

Where:

- Q is the global flow rate that goes through the porous medium (unit: $m^3 * s^{-1}$)
- S is the cross section of the sample which the fluid goes through (unit: m^2)
- k is the absolute permeability (unit: m^2)
- µ is the dynamic viscosity of the flowing fluid (unit: Pa*s)
- ΔP is the pressure difference applied around the sample (unit: Pa)
- L is the length of the sample in the flow direction (unit: m)
- $\frac{Q}{S}$ accounts for V, the superficial or mean fluid velocity through the porous medium

All the values of this equation can be deduced from the solution of the equation system (Q, ΔP) or are external conditions (S, L, µ).

Each core plug dataset consists of approximately 2 billion grid cells. Numerical computation using such a dataset far exceeds hardware limitations of even high-end computers. The software requires 146GB availability on RAM in order to perform such a computation. A projection on the hypothetical time it would take an 8-core computer with that kind of memory capability to calculate permeability for all three axes yields the unrealistic result of 200 days of simulation time per plug.

Since the computation of permeability for the entire (cropped) image volume is practically impossible, a sub volume needs to be established for the computations. This Region of Interest (ROI) as it is defined by the imaging software, needs to abide by the principle of Representative Elementary Volume (REV). REV is defined as the smallest volume over which a measurement can be made that will yield a value representative of the whole. Additionally, the selected ROI needs to be reasonably sized in terms of hardware requirements and time of simulation. Based on (Fernandes, 2012), the optimal ROI size that qualifies as REV in μCT images is 1400X1400X1400μm or 560X560X560voxels in size, with measurement stability being achieved for cubic ROIs with each dimension larger than 1000μm or 400voxels.

Based on the above information and after evaluating various ROI sizes (see chapter 4.3.3, Table 8), two different approaches were established for the selection of the appropriate ROI:

The first approach uses 20 small ROIs spread randomly within the imaged volume as seen in Figure 17. Each of the 20 ROIs has a dimension size of 427.5μm (or 171voxels), which represents 0.25% of the total volume. The sum of the total simulation size amounts to 5% of the total volume. The individual ROIs fall below the optimal REV range; however the inaccuracy of single measurements is expected to be mitigated by a statistically capable number of simulations coupled with a random spread over the volume. The ROIs are still large enough to capture the tortuosity and connectivity of the pore space (Mostaghimi, 2012).

The semi-random placement of the ROIs in the volume was based on the Latin Hypercube sampling method, which is a statistical method used to generate a sample of plausible collections of parameter values from a multidimensional distribution. The advantages of Latin Hypercube over true regular random sampling in such a distribution are twofold. Firstly, the sampling range is divided in equally probable intervals, with a forced division of equal samples over each interval. Additionally, random samples are taken one at a time, each time remembering which samples have already been selected so as to not repeat the same sampling (McKay, 1979). 20 different ROIs were sampled for each of the core plugs.

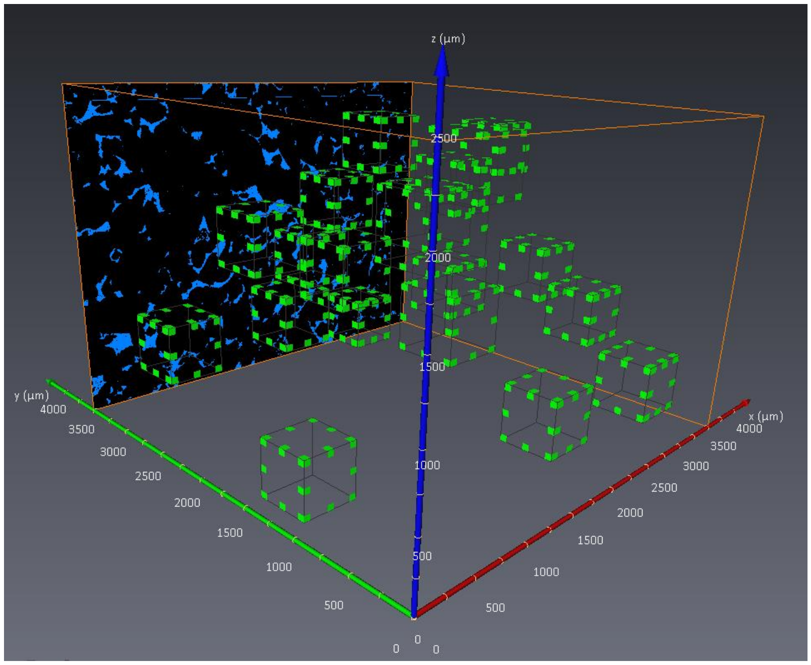

Figure 17: 3D Visualization of 20 Randomly Distributed ROIs within Imaged Volume

The second approach uses a single cubic ROI, centered within the total volume as seen in Figure 18. This ROI has a dimension size of 1250µm (or 500voxels). It represents 6.37% of the total imaged volume. Its size is well within the REV range, with however the disadvantage of constituting a single sample.

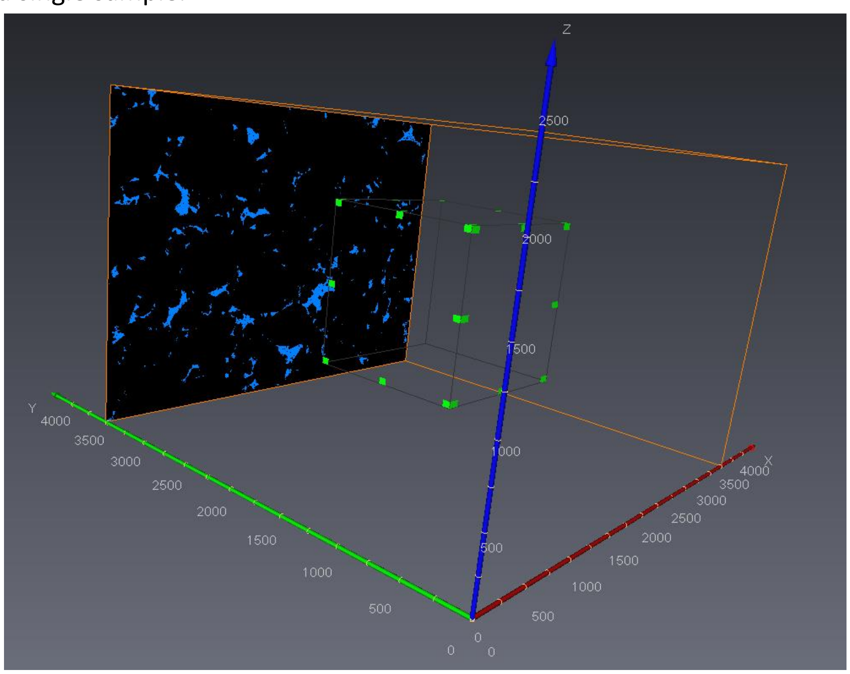

Figure 18: 3D Visualization of Single Centered ROI within Imaged Volume

In both approaches, the aforementioned solver was used in each of the specified ROIs to establish permeability in each of the three axes. The user specified control was decided to be the pre-specified input-output pressure. The input pressure was set to 49.6kPa, which was the maximum pressure applied by the micro-permeameter in analog testing, while the output pressure was set to 1.65kPa, which was the minimum pressure (leak off pressure) observed during micro-permeameter experiments. The viscosity of the modeled fluid was set to 0.001Pas. The convergence error criterion for the numerical simulations is by default set at 0.0001, and was not altered.

In order to evaluate pore network features of the imaged samples, further processing and analysis was conducted using Avizo. Three types of features make up the internal morphology of sedimentary rock samples:

- The grains that make up the solid phase.
- The individual pores that make up the majority of the void phase.
- The pore throats that traverse intergranular space, connecting the individual pores into a pore network.

The segmentation processing applied up to this point has distinguished between the solid and the void phase, registering them into one of two binary values accordingly. The objective of further segmentation in this research is to automatically detect and label individual features from the interconnected phase. An example of interconnected pore network can be seen in Figure 19 below.

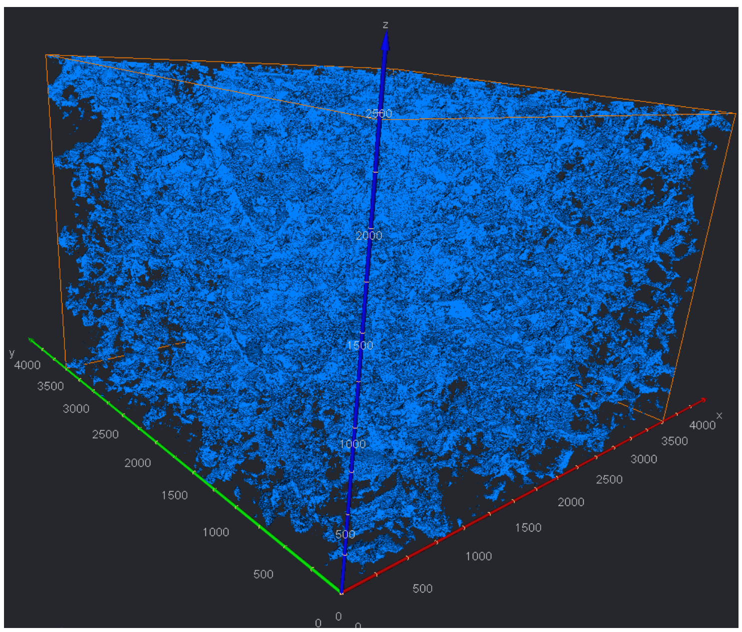

Figure 19: 3D Visualization of Pore Network of an Imaged Volume

The watershed algorithm is a highly automated segmentation method that sees widespread usage in image processing when it comes to automated objects segmentation or separation. It operates under the premise of a simulation of 'flooding' from a set of labeled regions in a 2D or 3D image. It expands those regions according to a priority map, defined by markers, until the watershed lines are reached. This process can be visualized as progressive immersion in a landscape, as seen in Figure 20 below.

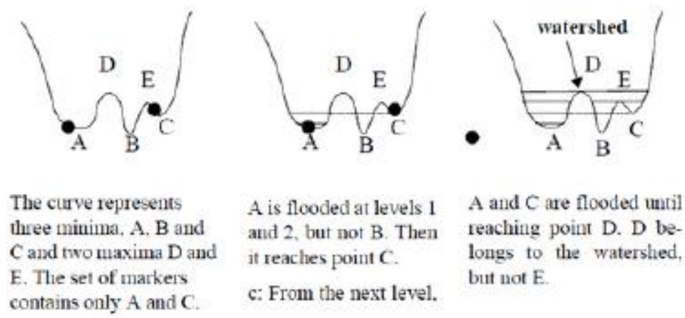

Figure 20: Visualization of Watershed Algorithm as Landscape Immersion (VSG, 1999-2013)

The algorithm requires two inputs:

1. A label image containing labeled marker regions that are used as seed areas for the flooding. At the end of the process, there will be as many separated objects as there are individual markers.
2. A grayscale image playing the role of the landscape height field or altitude map that controls the flood progression and finally the location of watershed separations. These separations are located on the crest lines between valleys of our landscape.

In order to apply the watershed separation on the various internal image features using Avizo, the Separate Objects module (or binseparate module in earlier versions) was used. The algorithm applies the watershed separation on each the binarized image stacks, using the respective original grayscale stack to compute the distance map. This distance map provides the priority map input for a watershed process. Maxima regions of the distance maps - the innermost areas of the pores - provide the markers input used for the watershed.

The resulting output consists of the desirable separation for grains and pores, visualized as the outline of each pore or grain. Subsequently each individual feature was labeled automatically in order for further analysis to take place. A 3D visualization of separated and labeled grains and pores can be seen below in Figures 22 (grains) and 23 (pores).

For pore throats, the watershed algorithm was first applied to separate the connected pores, enlarging the separation line width to 4 pixels in order for the throat to be discernible. Subsequently, an 'OR' logical operation was applied by another module using as input the image stack containing the defined pores, and the negative of the pore outline. This process can be visualized in Figure 21. The output is a qualitative interpretation of the pore throat. A 3D visualization of separated and labeled pore throats can be seen in Figure 24.

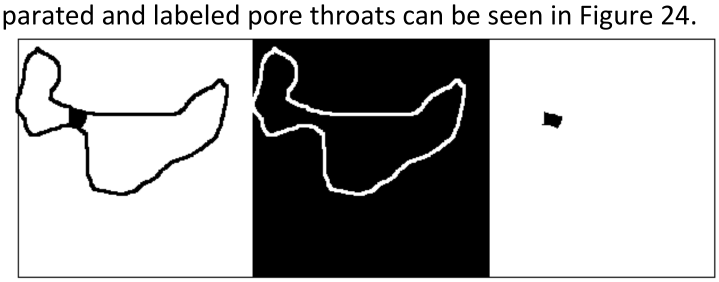

Figure 21 Left to Right: Separated Pores, Negative Pore Outline and Result of Logical Operation 'OR'

Subsequent analysis of the extracted features used the integrated Avizo analysis tool. For each feature, the location of its barycenter was specified in each of the three axes. For grains and pores, the 3D volume of each feature was measured as well. The output can be exported in Microsoft Excel spreadsheets for further processing.

Finally, a MatLab code was compiled that checks for features fully or partially included in each of the ROIs used for the simulation of permeability. The results can be found in 4.1.3, while the code ‘featurecheck’ can be found in the Appendix.

Further work was also conducted on determining the grain-size and pore-size distribution of the entire imaged volumes. The Equivalent Spherical Diameter of each particle (see Equation 3) was used as per common practice, in order to be able to also classify the structural material of the samples based on pore size distribution (ISO 14689-1:2003).

Equation 3: Equivalent Spherical Diameter

$$EqDiameter = \sqrt[3]{\frac{6 \times Particle3DVolume}{\pi}}$$

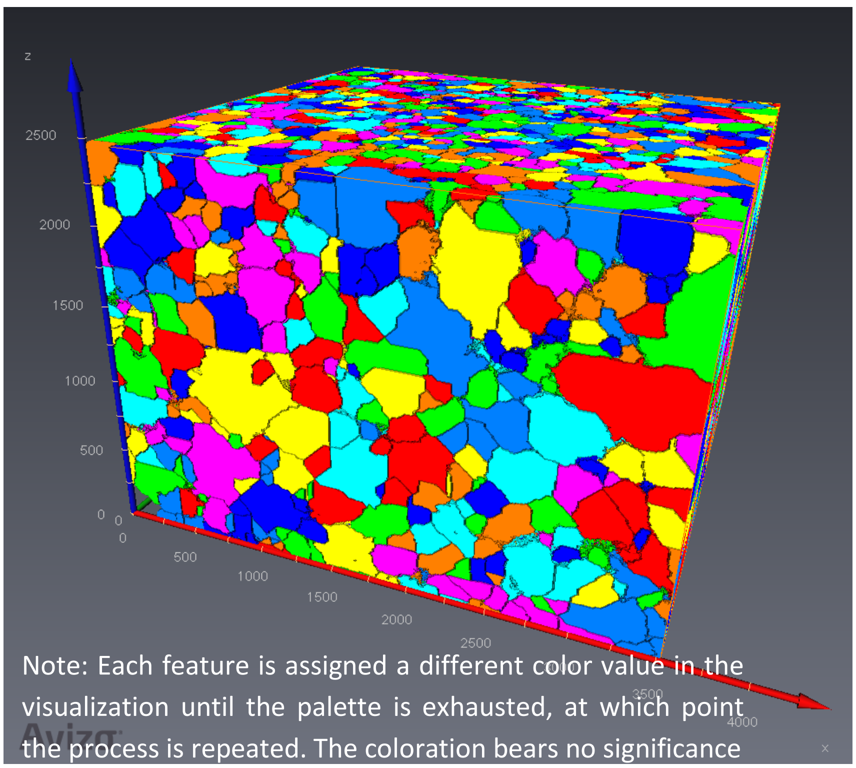

Figure 22: 3D Visualization of Separated Grains

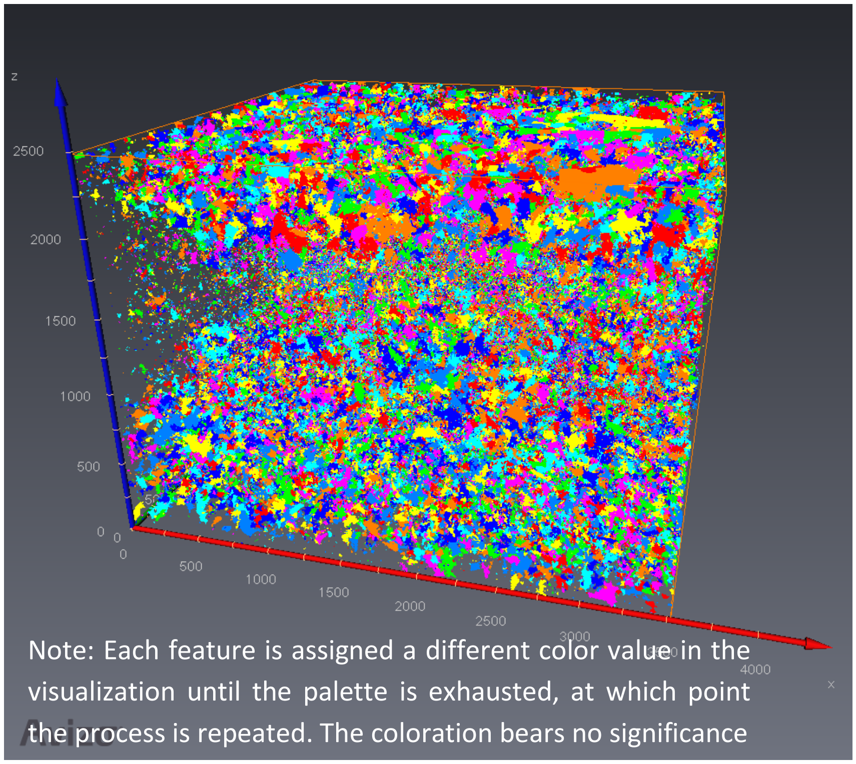

Figure 23: 3D Visualization of Separated Pores

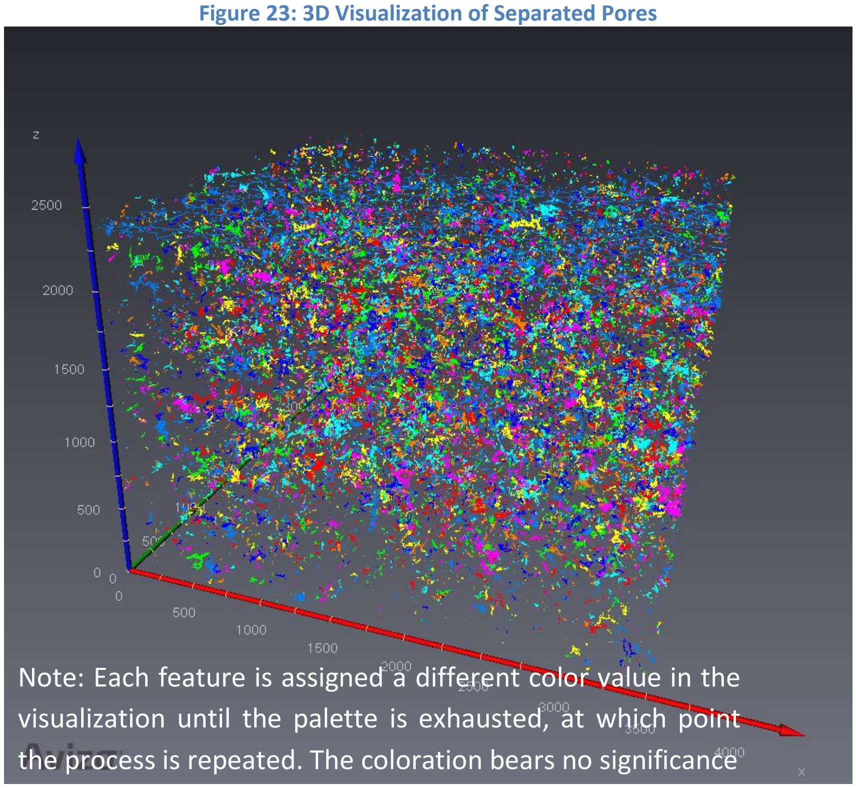

Figure 24: 3D Visualization of Pore Throats

3.2 Conventional Core Analysis

This chapter describes the conventional (analog) methods used to derive the porosity and permeability of the samples.

3.2.1 Analog Permeability

Probe (or mini-) permeameters are extensively used worldwide for making nondestructive permeability measurements on slabbed or nonslabbed cores from geologically complex, heterogeneous formations. The operation of these devices is based on the concept of flowing gas from the end of a probe sealed against the surface of a rock sample. Gas flows into the rock surface, the decay versus time is recorded and permeability is calculated from the pressure decay curve. The use of such devices to estimate local permeability is present in literature since 1959 (Dykstra, 1959).

Their usage is associated with many advantages, such as a fully computerized operation and a short measurement time (2-35 seconds per measurement). However, at the lower effective limit of their measurement range (1mD), the tests using conventional probe permeameters take a long time (over 20 minutes per measurement) and the results have a high uncertainty (50%). In order to address those problems, some modifications to the design of the original device were made which resulted in the creation of the Pressure Decay Profile Permeameter (Figure 25). (Jones, 1994). Information on the apparatus used can be found in the Appendix

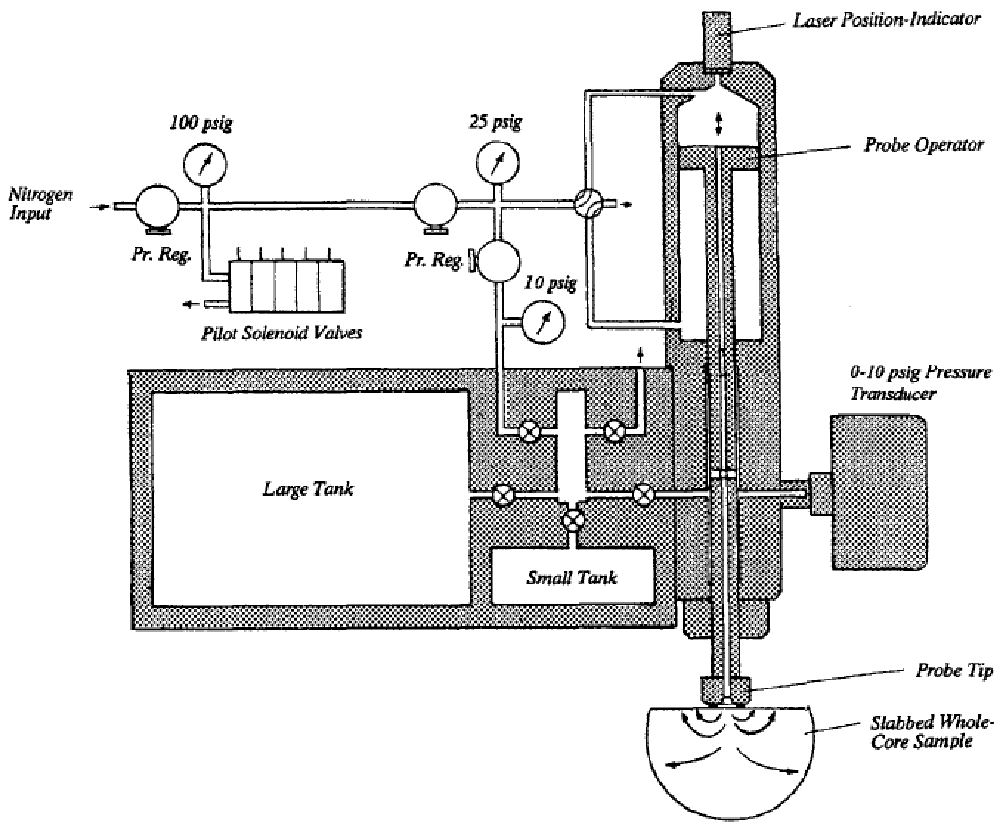

Figure 25: Sketch of Pressure Decay Profile Permeameter Components (Jones, 1994)

Initially, a set of calibration measurements was initially conducted in order to establish accuracy of the device and to familiarize with its operation. Seven benchmark plugs of known permeability (Figure 26) were measured to calibrate the machine.

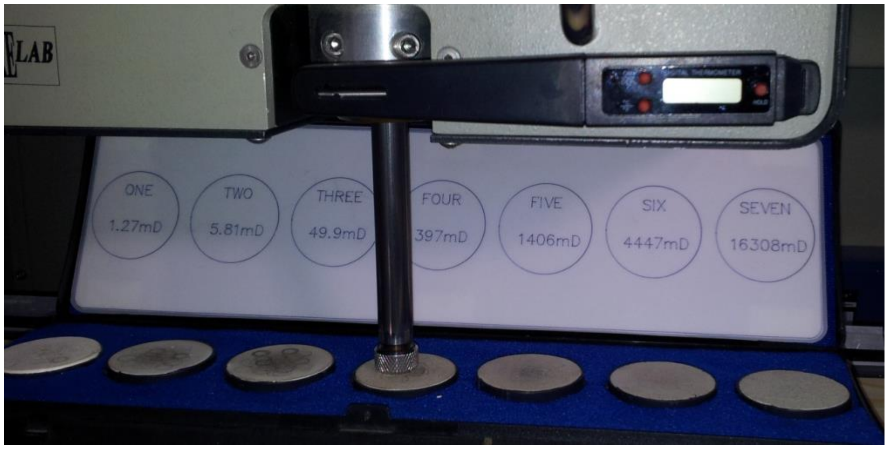

Figure 26: Permeameter Benchmark Plugs

Six measurements were acquired for each plug. The results were averaged and are shown in the following table.

Table 3: Permeameter Benchmarking Results

Sample	Known permeability (mD)	Average measured permeability (mD)	Absolute Error %
Benchmark Plug 1	1.27	1.02	20%
Benchmark Plug 2	5.81	4.6	21%
Benchmark Plug 3	49.9	41.4	17%
Benchmark Plug 4	397	374	6%
Benchmark Plug 5	1406	1463	4%
Benchmark Plug 6	4447	4752	7%
Benchmark Plug 7	16308	22400	37%

The device is more accurate in the middle part of its scanning range of 0.001 – 30000 mD, while for high and low permeable samples the error is significantly larger. An error of roughly 20% in the output results is taken into account during subsequent comparison with other results in 4.5.2.

The permeability measurements on the core plugs were conducted in two rounds.

In the first round of measurements, predating the extraction of the 'micro-plugs' from the core samples, a limited set of measurements was obtained (6 per plug). This was due to the fact that the probe requires a sealing facie. In the unprocessed plugs, sufficient sealing could only be achieved in one of the two surfaces shown in Figure 27. This is due to the irregular pseudo-convex curvature of one of those surfaces, as seen in the original sample photos, found in the Appendix.

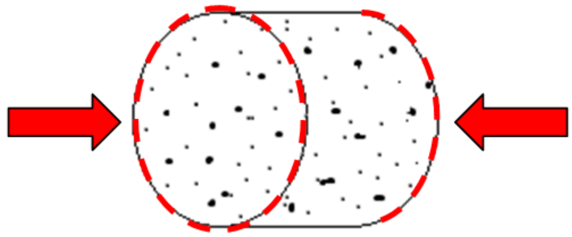

Figure 27: Measured Surfaces on the Original Plugs

The second round of measurements postdated the extraction of the aforementioned 'micro-plugs'. The cores were prepared in advance to include three flattened surfaces, with one of them oriented perpendicular to the other two (see Figure 27).

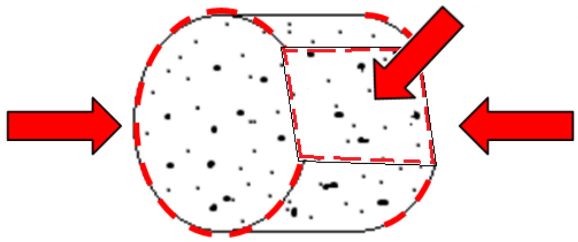

Figure 28: Measured Surfaces on the Processed Plugs

The second round of measurements yielded a larger, more statistically capable spread of measurements (20-21 per plug). Additionally the measurements of permeability were more spread out over multiple facies and axial orientations. The measurements are automatically Klinkenberg corrected by the micro-permeameter and are calculated through the use of the following equation (Equation 4). Additional output of the measurements includes an averaged pressure decline curve that indicates a pressure of 7.19 psi (or 49.6kPa) as maximum and 0.24 psi (1.65kPa) as minimum.

Equation 4: Permeability from Pressure Decay Permeameter (Jones, 1994)

$$k_\infty = \frac{29392\mu_g(p_1 + p_a)q_1}{(G_D r_i)\, p_1(p_1 + 2p_a + 2b)}$$

With:

k_∞: Klinkenberg permeability (slip-corrected), md

μ_g: gas viscosity, cp

p_1: upstream pressure (in probe), psig

p_a: ambient atmospheric pressure, psia

q_1: volumetric gas flow rate at upstream pressure and temperature, cm^3/s

r_i : inner probe-seal radius, cm

G_D: dimensionless geometric factor

b: Klinkenberg gas slippage factor, psi

3.2.2 Analog Porosity

In order to experimentally determine the porosity of the samples, an buoyancy/imbibition (water absorption, as per NBN EN 1936) method was utilised (WTCB, 2007). In such a method, immersing the porous sample in a (preferentially wetting) fluid under vacuum for a sufficiently long time will cause the fluid to imbibe to most of the interconnected pore space. The sample is weighed before (dry mass) and after the imbibition (submersed mass). These two weights, combined with the density of the fluid, permit calculation of the pore volume (Dullien, 1992). The bulk volume of the sample can be calculated rather accurately if the sample is prepared to very closely approximate a geometrical object.

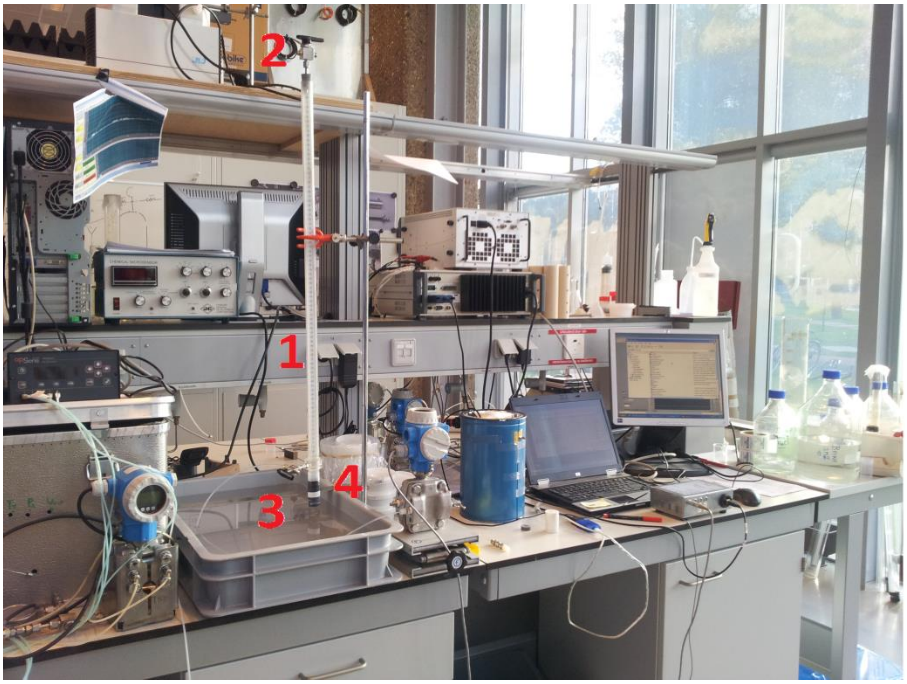

Figure 29: Analog Porosity Measurement Setup

The set up for the analog determination of porosity (Figure 29) consists of a sealed container (1), a valve used for evacuating air (2), a cup that initially holds the sample (3) and a weighing scale attached to a nylon cable ending into a small slipknot that will hold the sample (located at 4 – not shown here).

Prior to measurements the 5 micro-plug samples were prepared to very closely approximate a cylindrical shape so as to facilitate the measurement of their volume. Due to the method of their extraction they already have an almost entirely cylindrical shape so the only alterations were relevant to ensuring that both ends of each plug were flat surfaces perpendicular to the height of the cylinder.

Dry mass was measured for each micro plug. Afterwards, all of the micro plugs were placed in a vacuum and subsequently submersed in water. After that, the nylon cable was used to hold the 'micro-plugs', so that the submersed mass could be measured. Afterwards the porosity of the core can be measured through use of the following formula:

Equation 5: Experimental Porosity Calculation

$$\varphi = \left(1 - \frac{M_{dry} - M_{submersed}}{Volume * \rho_{water}}\right) * 100\%$$

In order to assess the accuracy of these measurements a simple error analysis method was applied on the calculating formula (Equation 5).

For each of the variables, the effect of small value deviations was assessed in terms of difference in results. Max cumulative error for deviation of the order of 10^{-3} SI units in volumetric (L, D), density (ρ_{water}) and mass (M_{dry}, $M_{submersed}$) measurements was calculated to be in the area of 22-25%. Due to the experimental nature of the method, instead of standard error calibration, error analysis was conducted in chapter 4.2.1 during result processing.

4. RESULTS

This chapter presents the results derived from image analysis. The results from the additional work done on feature extraction are presented here. After that the analog measurements on the same cores are shown, followed by a presentation of the associated logistics (computing requirements and timeframe). Finally, the results of the two analyses are compared amongst themselves and versus the original core test results from literature. The collective results from the original core run (NL Oil and Gas Portal) can be found in the Appendix.

4.1 Image Based Method Results

4.1.1 Porosity

The processing of the µCT stacks by ImageJ using the methodology described in 3.1 has yielded two porosity results for each of the five core samples. They can be seen below, in Table 4.

Table 4: Image Analysis Porosity Results

Sample	**CK1**	**CK2**	**CK3**	**CK4**	**CK5**
Voxel counting algorithm					
Pore Volume (mm^3)	1.375	2.672	1.304	0.159	1.096
Total Volume (mm^3)	30.909	30.909	30.723	30.785	30.692
3D Porosity	4.45%	8.64%	4.24%	0.52%	3.57%
Surface mesh based algorithm					
Pore Volume (mm^3)	0.594	1.909	0.86	0.01	0.013
Total Volume (mm^3)	30.904	30.909	30.723	30.779	30.686
3D Porosity	1.92%	6.18%	2.80%	0.03%	0.04%

The voxel counting algorithm results in a higher porosity, since all of the voxels defined as pore space are accounted for. The surface mesh based algorithm represents a more conservative estimation of the pore space, where isolated pore voxels or irregular pore voxels near the pore-matrix boundary are omitted as they are left outside the rendered pore volume.

4.1.2 Permeability

The results of the permeability simulations performed using Avizo (see 3.1.3) are presented below.

The single ROI method yielded three simulated results per core plug (one for each pair of axial inlets-outlets). They are presented in Table 5.

The 20 ROIs method produced 60 simulated results per core plug. This constitutes a statistically capable dataset which allows for observations regarding the frequency of occurrence of certain values within the value range. The can be sen below in Figure 30, while the collective result tables have been moved to the Appendix.

Table 5: Permeability Results Single ROI Method

Sample	Permeability X (Darcy)	Permeability Y (Darcy)	Permeability Z (Darcy)
CK1	0.0203	0.0186	0.0188
CK2	0.0669	0.0760	0.0762
CK3	0.0168	0.0162	0.0220
CK4	0.0184	0.0182	0.0183
CK5	3.8182	No percolating path	No percolating path

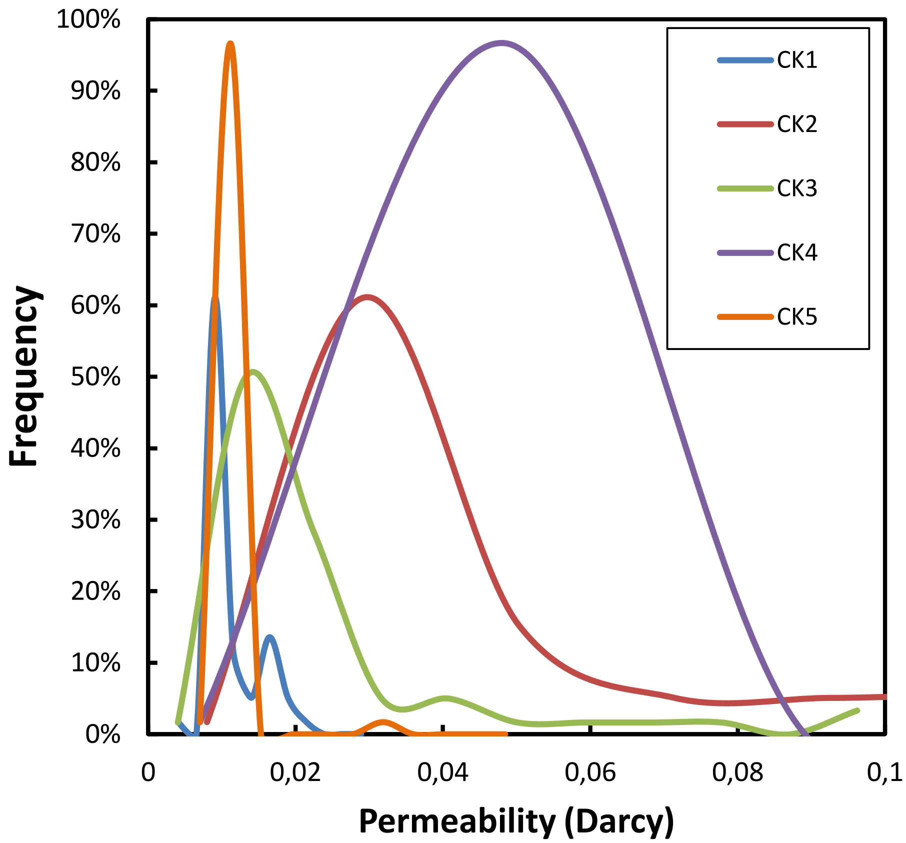

Figure 30: Distribution of Permeability Results using the 20 ROI Method (Frequency of Occurrence)

4.1.3 Grain - Pore - Pore Throat Analysis

The number of features in each of the permeability simulation ROIs (see 3.1.3) was accounted for. The following graphs (Figures 31 - 35) show of the number of features accounted for each sample using the 20 ROIs (171voxel sided cube). They are presented as frequency of occurrence distributions in order to be able to discuss homogeneity of features in 4.5.3. For the larger ROI (500voxel sided cube), singular measurements were obtained for each feature type and are presented in Table 6.

Table 6: Single ROI Method Feature Results

Sample	pores	grains	throats
CK1	45876	2373	12576
CK2	6600	799	2093
CK3	8948	984	1732
CK4	24396	1693	5325
CK5	99553	3145	35457

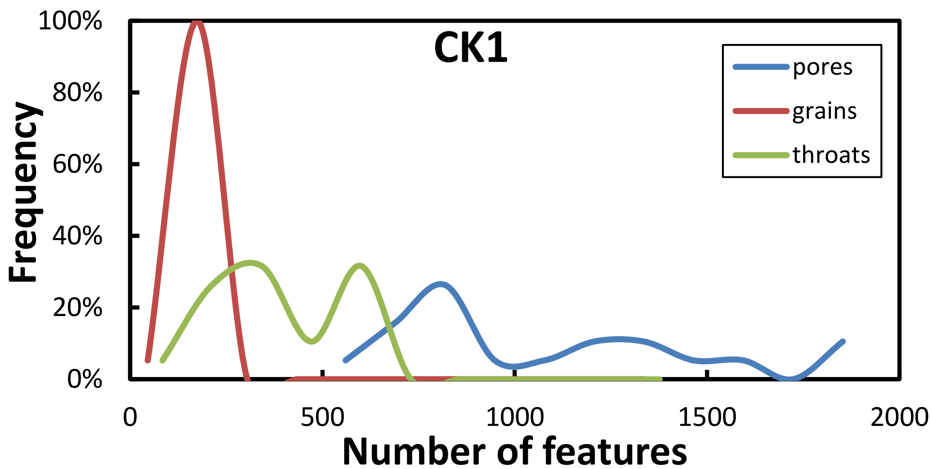

Figure 31: Distribution of Pores, Grains and Pore Throats in CK1 (Shown as Frequency of Occurrence in the Investigated ROIs)

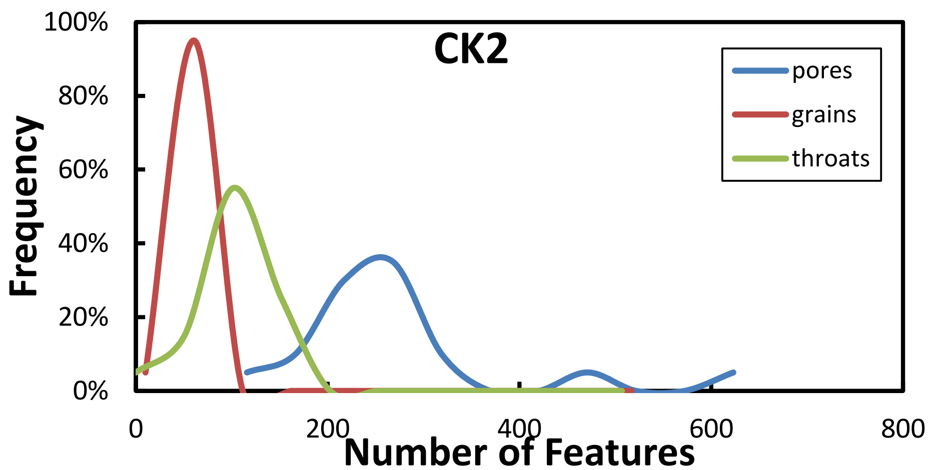

Figure 32: Distribution of Pores, Grains and Pore Throats in CK2 (Shown as Frequency of Occurrence in the Investigated ROIs)

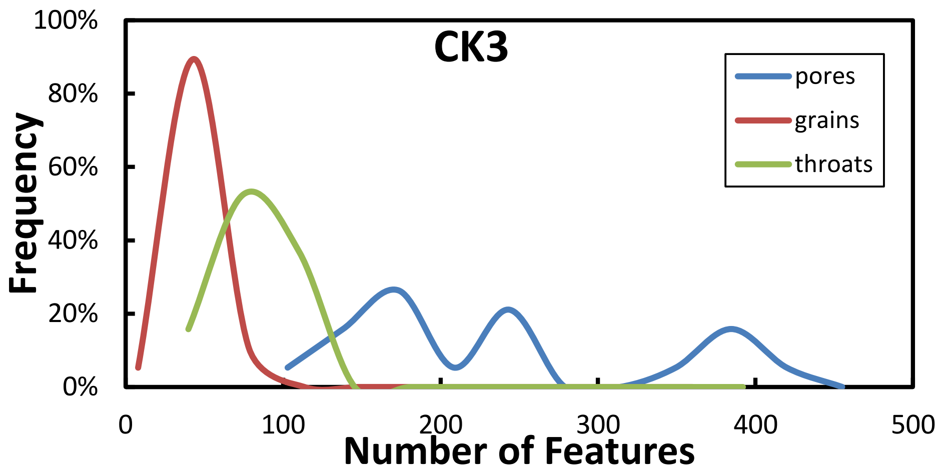

Figure 33: Distribution of Pores, Grains and Pore Throats in CK3 (Shown as Frequency of Occurrence in the Investigated ROIs)

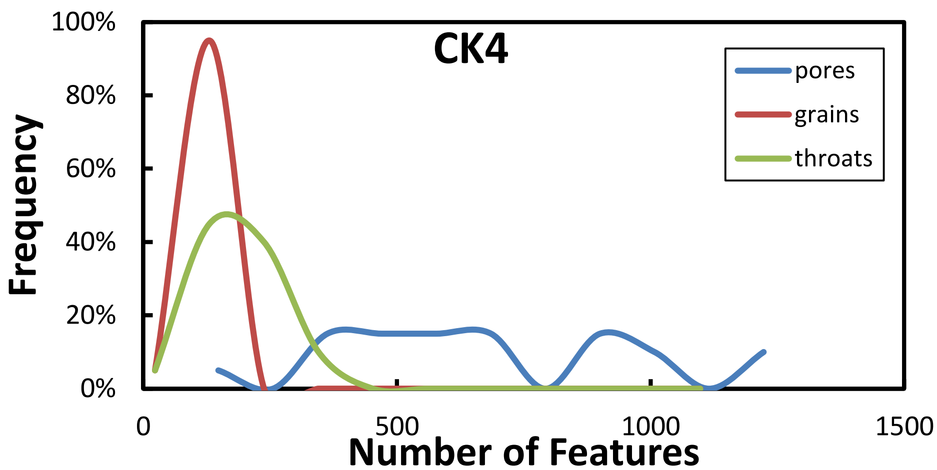

Figure 34: Distribution of Pores, Grains and Pore Throats in CK4 (Shown as Frequency of Occurrence in the Investigated ROIs)

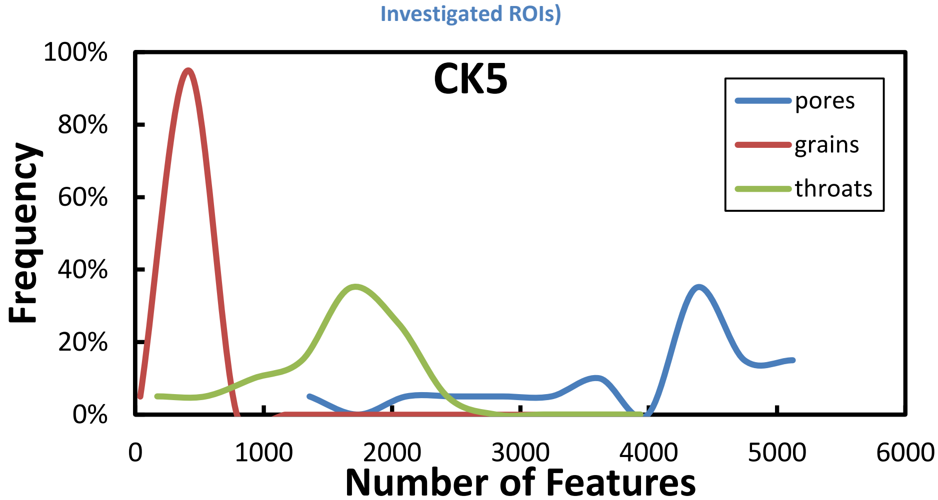

Figure 35: Distribution of Pores, Grains and Pore Throats in CK5 (Shown as Frequency of Occurrence in the Investigated ROIs)

4.1.4 Grain and Pore Size Distribution

Through advanced segmentation and image analysis (see 3.1.3), each of the features was accounted for, along with its 3D volume. After establishing the Equivalent Spherical Diameter (see Equation 3) of pores and grains, their size distribution throughout the entire volume of the samples was accounted for as a frequency. The two distributions are presented in the following graphs (Figures 36 and 37).

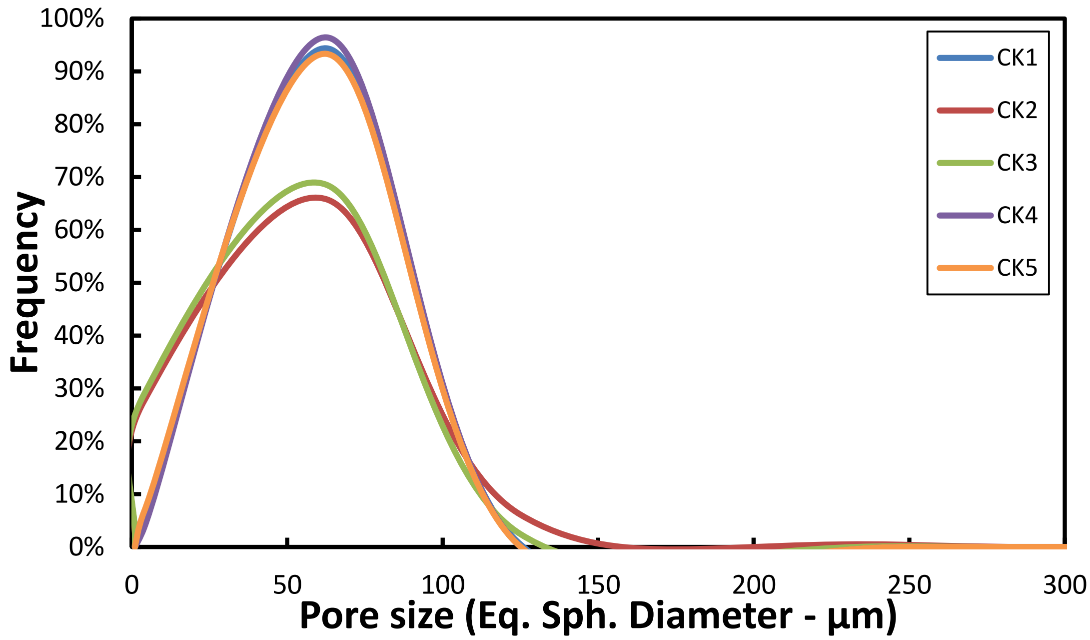

Figure 36: Pore Size Distributions within Imaged Volumes (shown as Frequency of Occurrence)

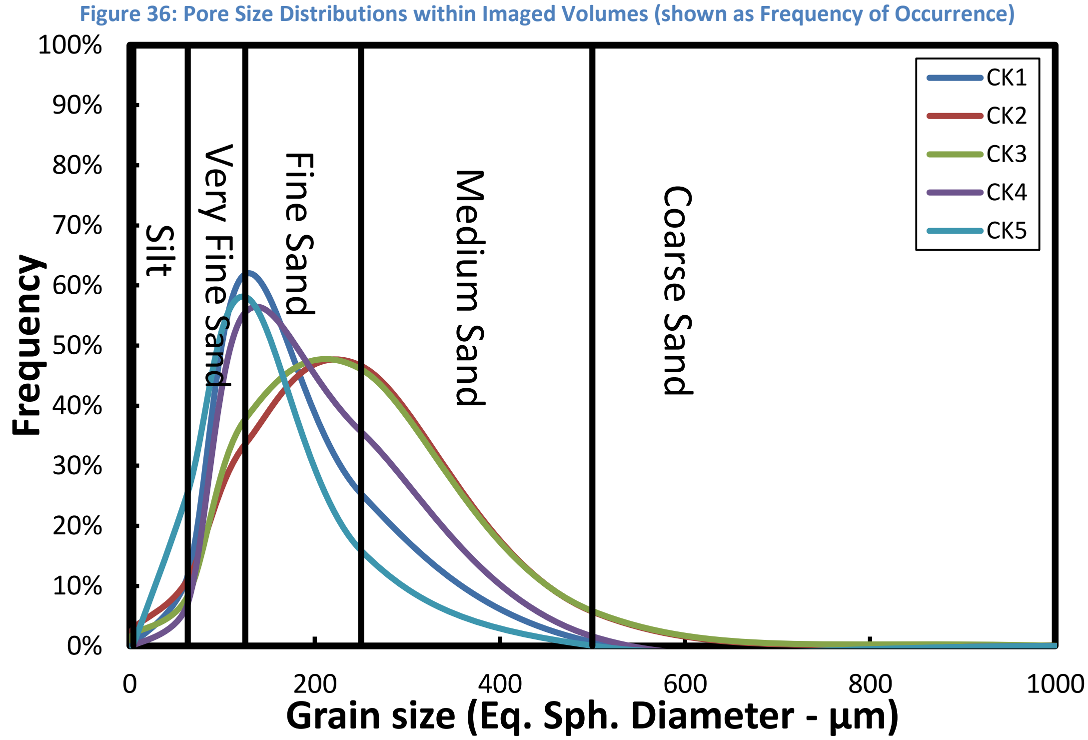

Figure 37: Grain Size Distributions within Imaged Volumes (shown as Frequency of Occurrence). Material classes according to International Standards (ISO 14689-1:2003)

4.2 Analog Measurement Results

The results of the conventional core analysis tests, conducted to assess the accuracy of the μCT scan based methodology, are presented below.

4.2.1 Porosity

Due to high shale/clay content, the CK5 micro-plug broke into two pieces during extraction from the core. Both pieces were prepared and measured individually. Their average is the value shown in Table 7 below. For each the other plugs a single porosity value was measured and is presented. Estimated error margin (see 3.2.2) is also presented for each measurement.

Table 7: Analog Porosity Measurement Results

Sample	Porosity	Error
CK1	6.3%	±1.6%
CK2	7.3%	±1.8%
CK3	7.6%	±1.9%
CK4	2.4%	±0.6%
CK5	5.9%	±1.5%

4.2.2 Permeability

The frequency distributions of the permeameter measurements can be seen in the graph below (Figure 38). The collective table of measurements can be found in the Appendix. The error is expected to range between 17% and 21% (see 3.2.1 – Table 3).

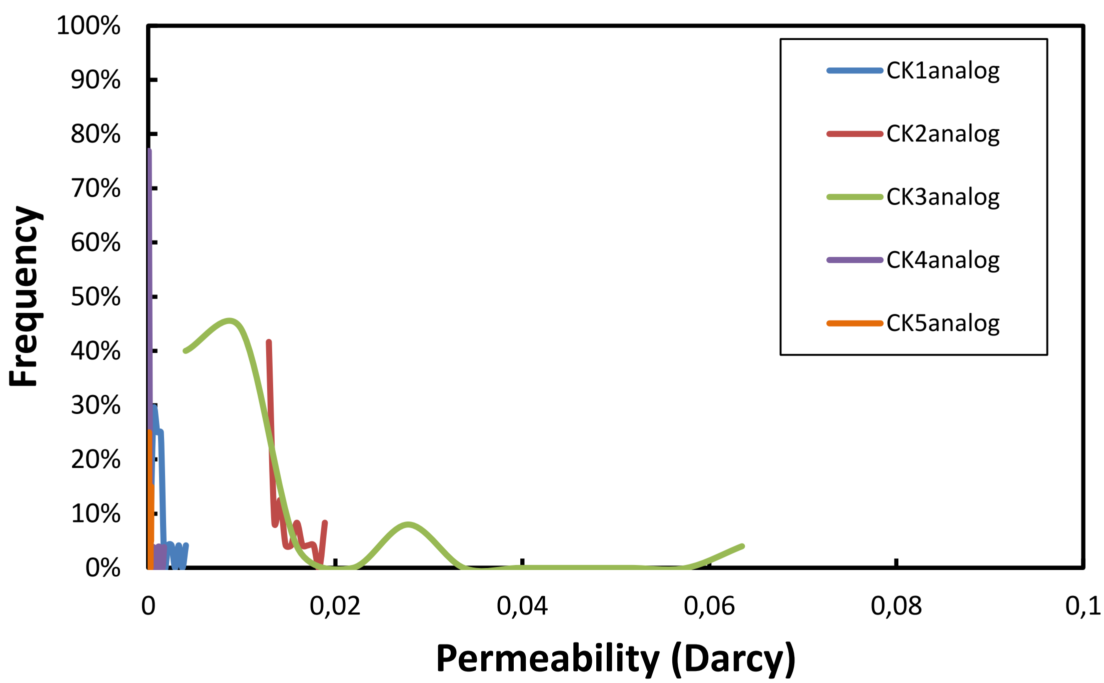

Figure 38: Analog Permeability Result Distributions

4.3 Logistics for Digital Analysis through μCT Imaging

Logistics comprise an important part of this thesis. They outline additional strengths and weaknesses of the proposed methodology, and provide the basis for discussion on improvements, to follow in 5.2. They are expressed briefly below through time logs and brief hardware description.

4.3.1 Acquisition

The scanning process lasts roughly 1 hour and 20 minutes per sample. Manual pre-processing using the scanner exportation software takes about 15-20 minutes per plug.

The associated digital hardware is a desktop workstation with a quad core processor and 32GBs of RAM, without external (non-processor integrated) GPU. Each of the exported image stacks at a resolution of 2.5 microns takes up 5-6 GBs in tiff format.

4.3.2 ImageJ

The time required from the point of importing the pre-processed result of the scan to the extraction of porosity measurements is 20 minutes per sample.

The hardware used is a desktop workstation with an 8-core processor and 16GBs of RAM, again without an external GPU. ImageJ is capable of multithreading, taking full advantage of multiple CPU configurations. RAM memory capacity is never exceeded during the process for a dataset this size, apart from the sole exception of when a 3D rendering visualization plug-in is used while both the grayscale input and the binary output are both loaded to memory.

The cropped and binarized image stack output is 1.7GBs per stack.

4.3.3 Avizo

Pertaining to availability of usage, both set-ups described above are used during Avizo operations. Like ImageJ, Avizo is capable of multithreading which translates to increased processing capabilities when using multicore workstations. With regard to the available hardware for this research, the computer used initially (8 core - 16GB RAM) was substituted for a slower computer set-up (4 core - 32GB RAM) when necessary in order to model larger ROIs, which require large RAM. All times below are given separately for the two hardware set-ups where applicable.

The time required to apply most core processes such as binary, logical and segmentation algorithms ranges between 10-15 minutes per sample (5-10 in the 8-core). Automatic labelling of features during analysis takes 10 more minutes regardless of hardware configuration. Exportation of the full feature measurements to excel ranges from 5 to 30 minutes per feature group (pore, grain, pore throat) per sample as it has to be done manually in sheets of 3333 measurements. Subsequently a MatLab routine is applied to include all of them in a compact format, which also takes 5-30 minutes depending on the data volume. The code 'autoappend' can be found in the Appendix.

Prior to the permeability tests, benchmark testing for various ROIs was conducted to determine the effect of increasing ROIs on processing parameters, as well as establish the practical limitations of the hardware. The quad core set up was used for benchmarking, and the results can be seen below, in Table 8.

Table 8: ROI Size Benchmarking for Avizo Permeability Simulations

ROI box dimensions [voxels]	ROI volume [μm^3]	ROI/Total image volume ratio [%]	ROI data size [MB]	Logged time (4-core set up) [minutes]	Logged time (8-core set up) [minutes]	RAM requirements [GB]
100 X 100 X100	1.56E+07	0.05	0.98	7	3	0.2
126 X 126 X 126	3.13E+07	0.10	1.95	9	4	0.2
159 X 159 X 159	6.28E+07	0.20	3.91	16	8	0.24
171 X 171 X171	7.81E+07	0.25	4.85	20	10	0.33
216 X 216 X216	1.57E+08	0.51	9.74	42	20	1
500 X 500 X 500	1.95E+09	6.37	119.93	360	180	6
3522,5 X 3522,5 X 2472,5 (entire volume CK3)	3.07E+10	100	140000	Not simulated	Not simulated	Not simulated

The permeability tests are a prime example of a process that is heavily dependent on processing capabilities of the hardware. The same benchmarking tests were conducted on the 8 core configuration and all of the logged times were roughly half the ones seen in the fifth column of Table 8 for the respective ROI sizes.

Permeability measurements using the twenty 171-pixel cubic ROIs took 3 hours 25 minutes inclusive of time spent in manually starting each simulation, per plug. The same measurements using a single centralized 500-pixel cubic ROI took 3 hours.

4.4 Logistics for Conventional Petrophysical Analysis

4.4.1 Porosity

Evacuation of the plugs within the sealed container before submersion requires 24 hours as per common practice. Subsequently, the measurement of porosity of the 5 micro-plugs lasted approximately 2 hours. This is a total of 26 hours.

4.4.2 Permeability

Each of the micro-permeameter measurements lasted 1-10 minutes, increasing for lower measured permeability. The total process for the first round of measurements (6 per plug) lasted 4 hours - inclusive of the operating learning curve - while the second round of measurements (20-21 per plug) lasted approximately 6 hours 30 minutes. In total, analog permeability measurements lasted 12-13 hours split up in two working days.

4.5 Discussion – Comparison of two Methods and Historical Data

Initially a result comparison of the proposed image analysis methodology and the conventional analysis methods is conducted. Subsequently, the results are evaluated versus data from the original core analysis (NL Oil and Gas Portal, 2013). As seen in Table 1, information as regards the originating depths of the cores is in the range of 1-3m (e.g.CK4:3649-3650m). As seen in the collective result tables in the Appendix, multiple results were recorded within that range, using various methods. Therefore, for the purposes of this comparison, the minimum and maximum values of each of the evaluated petrophysical properties are used for comparison, shown collectively below in Table 9.

Table 9: Minimum and Maximum Values of Petrophysical Properties from the Original Core Run

	Porosity (%)		Permeability (mD)	
Core Plug	**min**	**max**	**min**	**max**
CK1	6.1	12.9	0.1	32.8
CK2	11	13.3	5.88	323
CK3	3.8	13.8	0.34	86.1
CK4	2.5	5.9	0.01	0.05
CK5	2.1	5.1	0	0.44

4.5.1 Porosity

Voxel counting derived porosity closely matches analog tests, with difference in measurements ranging from 1.3% to 3.4% (Table 10). Results from the digital approach seem to underestimate porosity for the most part, with the exception of sample CK2, where the estimated porosity is higher. The surface mesh algorithm, though theoretically sound, appears to present overly conservative estimates, with difference in measurements ranging from 1.1% to 5.9% (Table 10).

Table 10: Comparison of Image Based and Analog Porosity Results

	CK1	CK2	CK3	CK4	CK5
3D Porosity Voxel counting	4,4%	8,6%	4,2%	0,5%	3,6%
3D Porosity Surface mesh	1,9%	6,2%	2,8%	0,03%	0,04%
Analog porosity	6,3%	7,3%	7,6%	2,4%	5,9%
Abs. Difference Analog - Voxel	1,8%	1,3%	3,4%	1,8%	2,3%
Abs. Difference Analog - Surface Mesh	4,3%	1,1%	4,8%	2,3%	5,9%

Considering the error typically associated with analog methods (see 4.2.1, Table 7), the results of the digital method are satisfactory. The scanned volume of roughly 30mm^3 does adequately represent the actual volume of 963-2095mm^3 of the micro-plugs. Inaccuracies in the digital determination of porosity can be traced in the 'loss' of pore voxels during the opening morphological operation, translatable to two types of features:

a) Non-percolating micro-porosity (disconnected small pores) that is eliminated by morphological erosion.
b) Convex pores of highly irregular geometries that are smoothened by the opening operation.

This loss explains why image measured porosity is lower than the analog measurements in most of the samples. The effect of the aforementioned morphological operation losses is particularly prominent in samples CK3 and CK5. In both of them a significant fraction of the total imaged porosity is predominantly composed of non-percolating micro-pores and irregular pores, features that are altered tor eliminated.

Results from both methods are also consistent with historical data from the original core run (see Table 9), with differences between current measurements and historical porosity data ranging between 0.1% and 11%.

4.5.2 Permeability

An observation to be made prior to the comparison of the two permeability measurement sets pertains to the importance of multiple applications of the method of measurement. As seen in both applied methods (in chapters 4.1.2 and 4.2.2), a series of measurements of permeability conducted under the same base settings, assumptions and boundary conditions does not warrant a single result or a very narrow range of values. Contrary to that, repetitive measurements distribute themselves over a wider range of values, following discernible curves that either closely approximate or are made up of a combination of standard continuous distribution patterns, such as bell shaped, triangular normal and logarithmic. Therefore, a statistically capable number of measurements need to be obtained regardless of methodology in order to correctly assess permeability in this scale.

Comparison of the permeability distributions resulting from the Avizo simulations - 20 small ROI variant - to the respective permeameter measurements shows the level of accuracy of the digital analysis. For CK3 (Figure 41), the results are very promising, as large parts of the two distributions are overlapping, with the most frequently occurring values also being very proximal. CK2 falls right behind (Figure 40) in terms of accuracy, followed by a less accurate match in CK1 and CK5 (Figures 39 and 43 respectively). The results for CK4 (Figure 42) are the least satisfactory, with regards to conformance to the experimentally measured permeability. It should be noted, however, that the maximum observed deviation of simulated permeability from analog measurements is 0.05 Darcy, with most differences between most frequent values ranging in the area of 0.01 Darcy.

There is no noticeable difference even if the permeameter error is considered. This is because according to Table 3 in chapter 3.2.1, the error is larger in scale for low-range permeability (roughly 20% for permeability<0.05 D), which produces very small differences if applied, and small for mid-range permeability (roughly 5% for permeability<0.44 D). Since there are no high-range measurements (permeability>1D) for which the scale of error is large and noticeable (37%), the overall accuracy of the comparison is within an acceptable margin.

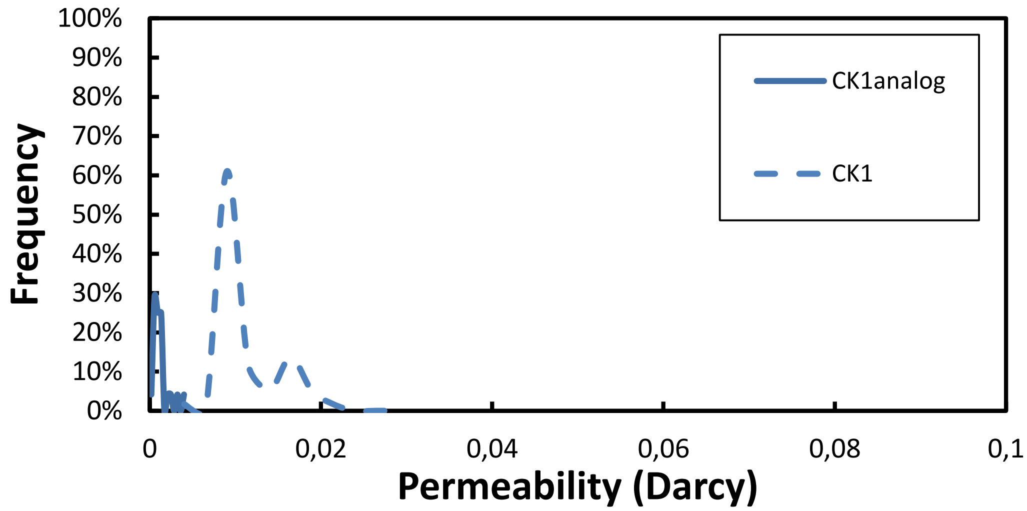

Figure 39: Comparison of Image Based (20 ROI Method) and Analog Permeability Results for CK1

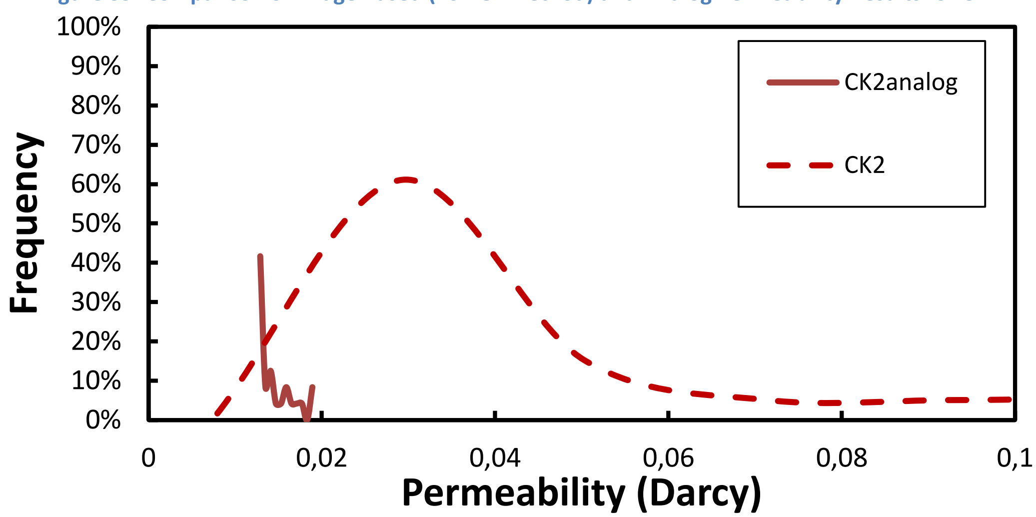

Figure 40: Comparison of Image Based (20 ROI Method) and Analog Permeability Results for CK2

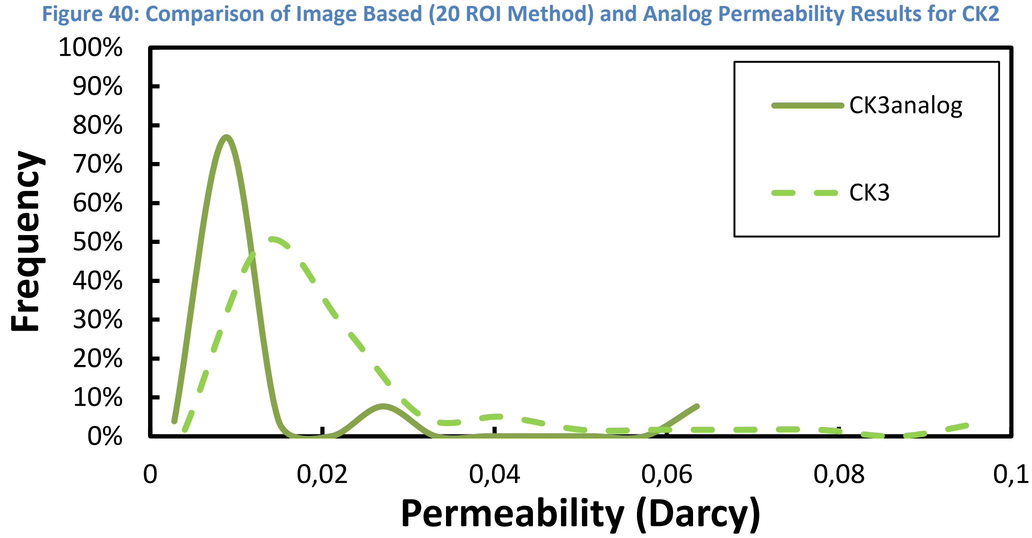

Figure 41: Comparison of Image Based (20 ROI Method) and Analog Permeability Results for CK3

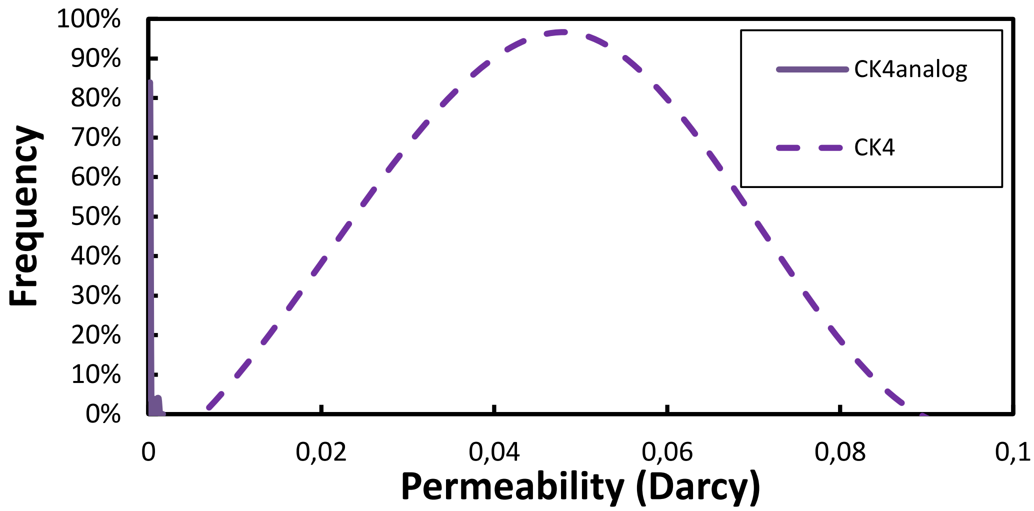

Figure 42: Comparison of Image Based (20 ROI Method) and Analog Permeability Results for CK4

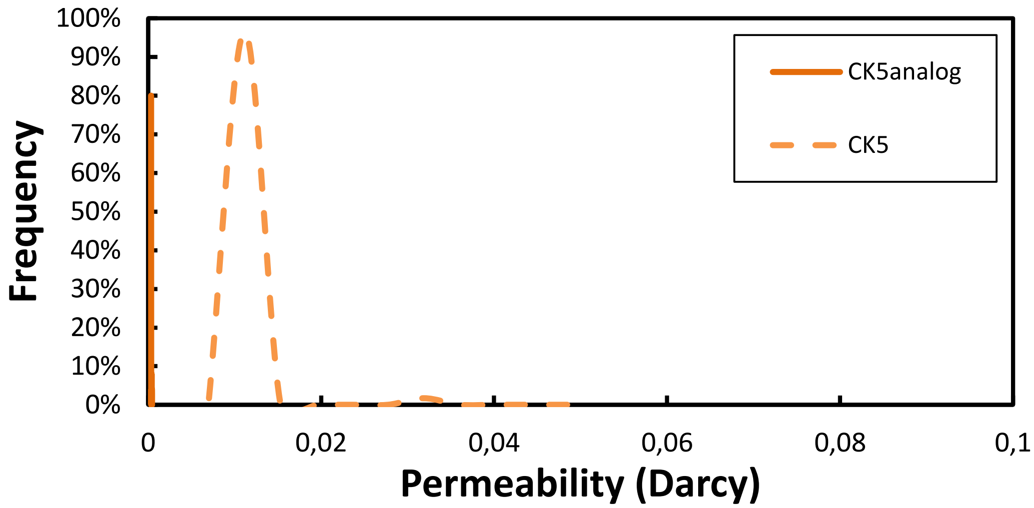

Figure 43: Comparison of Image Based (20 ROI Method) and Analog Permeability Results for CK5

For the single large ROI variant method there is a limited output of 3 directional simulations measurements per plug. Therefore they are used as a range compared versus the dominant frequency range (close to the frequency peak) of the analog measurements. As seen in Table 11, there is a noticeable deviation between the two methodologies in the more permeable sample (CK1). Also, the simulated results fail to establish a reasonable permeability range for CK5. For the rest of the samples, the deviation is relatively higher compared to the previously assessed approach (0.016-0.018 Darcy deviation compared to 0.01 D).

For CK2, the deviation can be attributed to a quite permeable ROI that does not accurately represent the total volume. For CK5, a micro-fracture included in the ROI results in a highly permeable simulated measurement in one direction, with the other directions producing a null result due to a non-percolating network. Finally, the relatively accurate simulated ranges for remaining 3 samples are perceived by the author as indicative of a higher homogeneity in the respective rock samples.

The failure of this method to closely approximate respective analog measurements further underlines the initial observation as to the importance of multiple simulations/measurements per sample.

Table 11: Comparison of Image Based (Single ROI Method) and Analog Permeability Results

Sample	Image Based Permeability (D)	Analog Permeability (D)	Maximal Difference (D)
CK1	0.0186-0.0203	0.006-0.0013	0.02
CK2	0.0669-0.0762	0.0129-0.0141	0.05
CK3	0.0162-0.022	0.0028-0.0089	0.01
CK4	0.0182-0.0184	0-0.0002	0.02
CK5	0-3.8	0-0.0003	3.8

As seen in Table 9, for most of the core plug intervals the historical data ranges are consistent with the respective results of the various tests conducted in this thesis. Historical measurements are localized in the range between 0 and 0.1 Darcy with the exception of CK2, which is exactly the case as regards the simulated permeability results.

4.5.3 Grain - Pore - Pore Throat Analysis

The number of grains seems to be consistent for all ROIs over the five sample volumes, following a triangular distribution for the most part. As regards separated pores, their number seems to largely fluctuate within the same sample which is indicative of micro-heterogeneity. The pore throats follow a distribution pattern similar to that of grains. Theoretically, samples that exhibit a higher number of pore throats should be more permeable, as the presence of more pore throats implies high interconnectivity between pore bodies. However, this is not the case here, with low permeability sample CK5 far surpassing more permeable samples such as CK2 (Chapter 4.1.3 - Figures 35, 32 respectively). This illustrates a weakness in the former assumption, since a large number of pore throats connecting micro-pores (such as in sample CK5) does not necessarily translate to a highly connected network. Thus the pore throat analysis is not taken into account when making qualitative assessments about the connectivity of the samples.

4.5.4 Grain and Pore Size Distribution

As seen in the graph (4.1.4 - Figure 37), the sorting of the constitutive granular material can give the following information on the origin of samples: CK2 and CK3 are sandstones from the same formation, CK1 and CK4 can either originate from sandstone or shale depending on cross correlation with other properties as well, and CK5 is most likely shale, based on the skewness of its distribution towards fine material ('silt' grade). The results are on par with what is expected from its originating stratigraphic unit, the Hardegsen Formation, which is comprised of alternating sandstones and claystones (DINOloket - Data en Informatie van de Nederlandse Ondergrond).

The pore size distribution (4.1.4 - Figure 36) is less accurate due to the fact that the assumption of Equivalent Spherical Diameter does not relate to their mostly concave shapes adequately. However, a similar pattern as the one seen in the grain size distribution can be seen.

4.5.5 Logistics (Time)

The time required for either combination of alternate approaches towards obtaining porosity and permeability using the µCT image analysis methodology is comparable to the time required by the analog measurements. This is considering a standardized but not automated process for the µCT method.

The following Table (Table 12) shows a comparison of the time required to measure permeability and porosity for each sample.

It should be noted that porosity and permeability measurements using the image analysis method can be conducted simultaneously, thus further reducing the overall time.

Conversely, the experimental method used for the determination of porosity in this thesis is not considered optimal in terms of time, but still falls within the average of methods used to measure porosity.

All things considered, analog measuring of the two properties is only marginally faster than the proposed methodology.

Table 12 - Comparison of Measurement Time per Sample for the two Methods

Image Analysis (minutes/plug)		**Analog Measurements (minutes/plug)**	
Process	**Time**	**Process**	**Time**
General		**General**	
Sample Preparation (milling of micro-plugs):	15		
µCT Acquisition:	100		
Porosity		**Porosity**	
ImageJ processing:	15	Sample Preparation (evacuation)*:	1440
Porosity extraction & Data Processing:	5	Measurement & Data Processing:	35
Permeability		**Permeability**	
Avizo processing & Simulations (20 ROI variant):	220	Processing (surface flattening):	10
Avizo processing & Simulations (Single ROI variant):	180	Measurement (20 results) & Data Processing:	60
Permeability extraction & Data Processing:	5		
Total time (20 ROI variant):	**360**	**Total time (inclusive of evacuation):**	**1545**
Total time (Single ROI variant):	**320**	**Total time (exclusive of evacuation):**	**105**
*Evacuation time is the same regardless of number of samples.			

5. CONCLUSION & OUTLOOK

The conclusive chapter of this thesis is structured in three parts. The first part contains a commentary on the efficiency of the methodology, tapping into the results discussion (chapter 4.5) for reference. The second part identifies areas of improvement for the methodology. The third and final part is a more general outlook on the future of such a methodology in petrophysical evaluation.

5.1 Result Commentary

A relatively good match of image based and analog porosity measurements has been obtained. Voxel counting is optimal at this resolution, while the surface mesh algorithm gives better results for more porous samples. However, the method needs to be improved towards the margin of difference from analog measurements. This becomes more prominent in samples of low porosity such as the ones evaluated in this thesis, where a difference of 2-5% is very significant.

As regards permeability, simulated and analog measurements are also relatively closely matched. Qualitatively, there is a match between the distribution curves, but the image based method is still lacking in accuracy for determining the permeability of the less permeable formations, and is prone to errors. The results also underline the importance of statistically capable sampling and volumetrically distributed measurements over large ROI sizes.

The distinction of morphological features is less accurate. Still, the method gave fairly good results as regards pore size distribution towards the determination of lithology

All things considered, the methodology has characterized the rock samples based on solely extracted µCT scan data within an acceptable margin of error. This methodology is structured to follow a standardized process path, with no constraints as to the origin of the samples. In this thesis, relatively 'tight' samples were investigated; better results are expected in the evaluation of samples of more porous and/or percolative nature.

Direct advantages of the proposed methodology over conventional petrophysical analysis pertain to the nature of the dataset. To elaborate further, there are three advantages associated with µCT images, exclusive to image based methods:

- The digital nature of the extracted dataset makes archiving easier by separating the digital imprint of the sample for its physical form. Additionally, as new tests and more refined (image based) methods become available, the dataset is always available for re-evaluation and new measurements.
- The digital form of the dataset also facilitates copying and sharing. This means that not only individual properties can be measured simultaneously over multiple computers, but also that the dataset can be shared globally over specialized business research units and/or academic institutions.
- The method has no need for specialized hardware past the imaging (µCT) setup.

5.2 Areas of Improvement

Since the proposed methodology is based on a sequence of discreet processes, it is important to evaluate areas of improvement on each of them individually.

- The Image acquisition and preprocessing stage can benefit from a more thorough investigation of filtering and artifact reduction options. Hardware capabilities of a CT scanner of equal or better capabilities in terms of imaging resolution are on par with the requirements of the methodology. Further refinement of the voxel size will result in more accurate images but also significantly larger datasets.
- Image processing can benefit from more sophisticated threshold selection methods. In their paper K. J. Batenburg and J.Sijbers (Sijbers, 2009) discuss the adoption of an algorithm that is based on projection data rather than processed tomogram data, that shows results superior to established histogram-based methods (Otsu's method and the like). Additionally, during further image segmentation it was established that the watershed algorithm does not properly account for convex shapes and also warrants investigation.
- Image analysis benefits mainly from advances in hardware capabilities and automation. As regards hardware capabilities, increased processing speed -Moore's Law predicts a doubling of processing speed every 2 years (Moore, 1965)-, multi-core capabilities, and dedicated GPUs (Graphics Processing Units) greatly hasten individual tasks while increased RAM capabilities allow for larger maximal sizes of datasets to be processed. As regards automation, both ImageJ and Avizo support integrated scripting, which can facilitate user interaction by automating entire process sequences such as feature extraction or chain multiple permeability simulations.

The theoretical elements pertaining to the digital identification of porosity and permeability are also subject to potential improvement.

- As regards porosity direct voxel counting gives good results. However, the surface mesh generation algorithm can potentially be just as accurate, or even superior in the accurate prediction of porosity. As stated by the BoneJ plugin developers, the 'Marching Cubes' rendering algorithm is used towards rendering the reconstructed pore volume. In the paper describing the algorithm (Lorensen, 1987), towards the conclusive remarks the developers already advertize the superior nature of a 'Dividing Cubes' algorithm they are working on. Considering the original paper is from 1987, it is the authors belief that more sophisticated algorithms have been developed since, and further investigation is pending as to their application in image analysis software.
- In their paper, Z.R. Liang, P.C. Philippi, C.P. Fernandes, AND F.S. Magnani (Liang, 1999) proposed a variant process towards the determination of permeability from digital images using topological features (skeletonized pore network).

5.3 Outlook

Expansion of the range of petrophysical properties is a matter of developing the theoretical link between physical property and 3D image. The methodology is also used to extract information on the distribution of mineral content in rock samples, based on the difference in grayscale response from mineral components of different densities. 3D data of this kind can assist in geologic interpretation during reservoir development and rock genesis studies, as well as find practical applications in other relevant fields such as mining.

A common undertone along the presentation of this methodology has been the interdisciplinary origin of many of the constituting theoretical and practical elements. In order for this kind of digital approach to petrophysical evaluation to really take off, it is the author's opinion that direct cooperation with specialist engineering and scientific disciplines will have to become the norm.

For example, a lot of progress in the processing and analysis of μCT scans is continuously being made by the medical community; as regards rendering algorithms and efficient management of hardware resources towards software intensive applications, the computer gaming industry defines the state of the art.

Looking further into the future, a fully automated methodology that accepts samples as input and gives direct petrophysical property measurements as output is foreseeable.

Even further into the future, a potential decrease in the cost and the footprint of μCT scanners (though not likely in the very near future) will mean that more widespread use of purely digital core analysis will constitute the norm.

Finally, moving towards the broader scale, it can also be argued that better understanding of the pore/permeability network offered by image based methods will positively influence the selective application of specialized Enhanced Oil Recovery methods in the future.-

Bibliography

Akin, S. K. (2003). *Computed tomography in petroleum engineering research.* London: Geological Society.

Al-Ansi, N. ,. (2013). Influence of Micro-Computed Tomography Image Resolution on the Predictions of Petrophysical Properties. *IPTC 16600.* Beijing, China.

Al-Kharusi, A. S. (2006). Network extraction from sandstone and carbonate pore space images. *Journal of Petroleum Science and Engineering*.

Al-Raoush, R. ,. (2005). Extraction Of Physically Realistic Pore Network Properties From Three-Dimensional Synchrotron X-Ray Microtomography Images Of Unconsolidated Porous Media Systems. *Journal of Hydrology*.

Arns, C. H. (2004). Virtual permeametry on microtomographic images. *Journal of Petroleum Science and Engineering 45*.

Cnudde, V. (2005). *Exploring The Potential Of X Ray Tomography As A New Non Destructive Research Tool In Conservation Studies Of Natural Building Stones.* universiteit Gent.

Darcy, H. (1856). Les Fontaines Publiques de la Ville de Dijon. Dalmont, Paris.

Degruyter, W. (2005-2006). *Exploring the potential of digital image analysis of SEM and Micro-CT images of accretionary lapilli.* Universiteit Gent.

DINOloket - Data en Informatie van de Nederlandse Ondergrond. (sd). Opgehaald van http://www.dinoloket.nl/hardegsen-formation-rbmh

Dong, H. (2007). *Micro-CT Imaging And Pore Network Extraction.* London: Imperial College.

Doube M, K. M.-C. (2010). BoneJ free and extensible bone image analysis in ImageJ. *Bone 47:1076-9*.

Dullien, F. (1992). *Porous Media. Fluid Transport and Pore Structure.* Academic Press.

Dykstra, H. a. (1959). *The Prediction of Oil by Waterflood, Secondary Recovery of Oil in the United States.* New York City: API.

Fens, T. J. (1991). Automated mineral identification of sandstone samples using sem/image analysis techniques. *SCA Symposium on Core Analysis, vol. 1, no. 9109*, (p. 24). London, UK.

Fens, T. W. (2000). *Petrophysical properties from small rock samples using image analysis techniques.* TUDelft.

Fernandes, J. S. (2012). Determination of the Representative Elementary Volume for the Study of Sandstones and Siltstones by X-Ray Microtomography. *Materials Research. 2012; 15(4)*, 662-670.

Hildebrand, T. L. (1999). Direct Three-Dimensional Morphometric Analysis of Cancellous Bone. *Journal Of Bone And Mineral Research*.

ISO 14689-1:2003. (sd). *ISO/TC 182/SC 1*.

Jones, S. C. (1994). A New, Fast, Accurate Pressure-Decay Probe Permeameter. *SPE Formation Evaluation*.

Liang, Z. ,. (1999). Prediction of Permeability from the Skeleton of Three-Dimensional Pore Structure. *SPE Reservoir Eval. & Eng. 2*.

Lorensen, W. E. (1987). Marching cubes: A high resolution 3D surface construction algorithm. *Computer Graphics, Volume 21, Number 4*.

McKay, M. D. (1979). A Comparison of Three Methods for Selecting Values of Input Variables in the Analysis of Output from a Computer Code. *Technometrics Vol. 21, No. 2*, 239-245.

Moore, G. E. (1965). Cramming More Components onto Integrated Circuits. *Electronics*, 114–117.

Mostaghimi, P. B. (2012). Computations of Absolute Permeability on Micro-CT. *Mathematical Geosciences*.

NL Oil and Gas Portal. (2013, 10 10). Opgehaald van http://www.nlog.nl/

Otsu, N. (1979). A Threshold Selection Method from Gray-Level Histograms. *IEEE Transactions on Systems, Man, and Cybernetics, Vol. SMC-9, No. 1*, 62-66.

Prince, C. M. (2002). Predicting Rock Properties From Digital Core Images. *SCA2002-34.* International symposium, Society of Core Analysts.

Saites, F. W. (2006). Coalbed Characterization Studies With X-Ray Computerized Tomography (CT) and Micro CT techniques. *Petroleum Society, Paper 2006-027.*

Sankur, M. S. (2004). Survey over Image Thresholding Techniques and Quantitative Performance Evaluation. *Journal of Electronic Imaging 13*, 146-165.

Schindelin, J. A.-C. (2012). Fiji: an open-source platform for biological-image analysis. *Nature Methods 9*, 676-682.

Shin, H. (2002). *A throat finding algorithm for medial axis analysis of 3D images of vesiculated basalts.* State University of New York at Stony Brook.

Siddiqui, M. S. (2009). Advances in Micro-CT Based Evaluation of Reservoir Rocks. *SPE 126039.*

Sijbers, J. B. (2009). Optimal Threshold Selection For Tomogram Segmentation By Projection Distance Minimization. *IEEE Transactions On Medical Imaging, Vol.28, No.5*, 676-686.

Smith, S. W. (2013, 10 12). *The Scientist and Engineer's Guide to Digital Signal Processing*. Opgehaald van http://www.dspguide.com/ch25/4.htm

Stokes., G. (1845). Transactions of the Cambridge Philosophical Society. In *volume 8* (pp. 287-305).

The Science Education Resource Center at Carlton College. (2013, 10 12). Opgehaald van http://serc.carleton.edu/images/research_education/geochemsheets/techniques/_1172960774.png

VSG, V. S. (1999-2013). Avizo User's Guide.

WTCB. (2007). Beproevingsmethode voor natuursteen. Bepaling van de werkelijke dichtheid, de schijnbare dichtheid en van de totale poreusheid. *NBN EN 1936*.

Youssef, S. B. (2008). Pore Network Models Combined To High Resolution Micro-Ct To Assess Petrophysical Properties Of Homogenous And Heterogenous Rocks. *IPTC 12884-MS.*

Zhang, S. B. (2011). Porosity And Permeability Analysis On Nanoscale FIB-SEM 3D Imaging Of Shale Rock. *SCA Symposium 2011.* Austin, Texas.

APPENDIX

µCT Scanner - phoenix nanotom S

Specifications	
Max. tube voltage	180 kV
Max. output	15 W
Detail detectability	Up to 200nm (0.2µm)
Min. focus-detector-distance	0.4mm
Max. voxel resolution (depending on object size)	< 500nm (0.5µm)
Geometric magnification (3D)	1.5 times up to 100 times
Max. object size (height x diameter)	150mm x 120mm / 5.9" x 4.7"
Max. object weight	2 kg/ 4.4 lb
Image chain	5-Megapixel fully digital image chain
2D X-ray imaging	no
3D computed tomography	yes
Advanced surface extraction	yes (optional)
CAD comparison + dimensional measurement	yes (optional)
System size	(1640 x 1430 x 750 mm), (64.6” x 56.3” x 29.5”), larger cabinets on request
System weight	1300kg / 2866 lb
Radiation Safety	- Full protective radiation safety cabinet according to the German RöV (attachment 2 nr. 3) and the US Performance Standard 21 CFR 1020.40 (Cabinet X-ray Systems)
	- Exposure rate < 1 µSv/h emission limit measured at 10 cm distance from accessible surfaces

Featurecheck MatLAB code

```
clc;
clear all;
close all;
%%read the ROI xls
%ck1
%data = xlsread('Permeability Large Box.xlsx','CK1');
%ck2
%data = xlsread('Permeability Large Box.xlsx','CK2');
%ck3
%data = xlsread('Permeability Large Box.xlsx','CK3');
%ck4
data = xlsread('Permeability Large Box.xlsx','CK4');
%ck5
%data = xlsread('Permeability Large Box.xlsx','CK5');

%read the feature xls - CHANGE SHEET No MANUALLY DUE TO CK5 OVER BOUNDS
grain = xlsread('grainsizes.xlsx','CK4');
pores1 = xlsread('pores.xlsx','CK4');
porethroats = xlsread('porethroats.xlsx','CK4');
%pores2 = xlsread('pores.xlsx','CK5part2');


%%check for each box - grains
graincounter = zeros(1,20);
checkgrain = zeros(length(grain),20);
for i=1:20
checkgrain(:,i) = grain(:,4)>data(i,14)&grain(:,4)<data(i,15)&...
grain(:,5)>data(i,16)&grain(:,5)<data(i,17)&...
grain(:,6)>data(i,18)&grain(:,6)<data(i,19);
graincounter(i) = sum(checkgrain(:,i));
end


%%check for each box - pores1
porecounter1 = zeros(1,20);
checkpores1 = zeros(length(pores1),20);
for i=1:20
checkpores1(:,i) = pores1(:,4)>data(i,14)&pores1(:,4)<data(i,15)&...
pores1(:,5)>data(i,16)&pores1(:,5)<data(i,17)&...
pores1(:,6)>data(i,18)&pores1(:,6)<data(i,19);
porecounter1(i) = sum(checkpores1(:,i));
end

porecounter2 = zeros(1,20);

%ONLY USED FOR CK5part2
%check for each box - pores2
%checkpores2 = zeros(length(pores2),20);
%for i=1:20
```

```
%checkpores2(:,i) = pores2(:,4)>data(i,14)&pores2(:,4)<data(i,15)&...
%pores2(:,5)>data(i,16)&pores2(:,5)<data(i,17)&...
%pores2(:,6)>data(i,18)&pores2(:,6)<data(i,19);
%porecounter2(i) = sum(checkpores2(:,i));
%end


 %%check for each box - porethroats
throatcounter = zeros(1,20);
checkthroat = zeros(length(porethroats),20);
for i=1:20
checkthroat(:,i) =
porethroats(:,4)>data(i,14)&porethroats(:,4)<data(i,15)&...
porethroats(:,5)>data(i,16)&porethroats(:,5)<data(i,17)&...
porethroats(:,6)>data(i,18)&porethroats(:,6)<data(i,19);
throatcounter(i) = sum(checkthroat(:,i));
end

 porecounter = zeros(1,20);
for i=1:20
  porecounter(i)= porecounter1(i) + porecounter2(i);
end

output=cell(21,4);
output(1,2)={'pores'};
output(1,3)={'grains'};
output(1,4)={'throats'};
for i=2:21
output(i,1)= {strcat('box',num2str(i-1))};
output(i,2)={porecounter(1,i-1)};
output(i,3)={graincounter(1,i-1)};
output(i,4)={throatcounter(1,i-1)};
end

xlswrite('featurechecklarge.xls', output, 1, 'a1')
```

Core Sample Photos

CK1

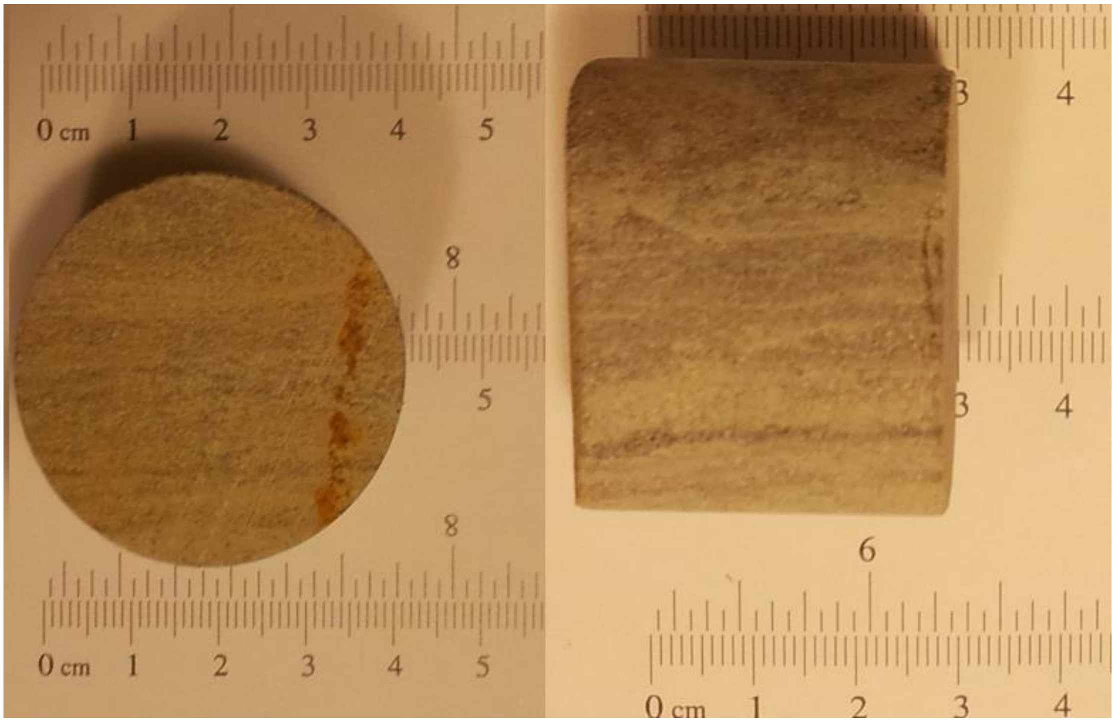

CK2

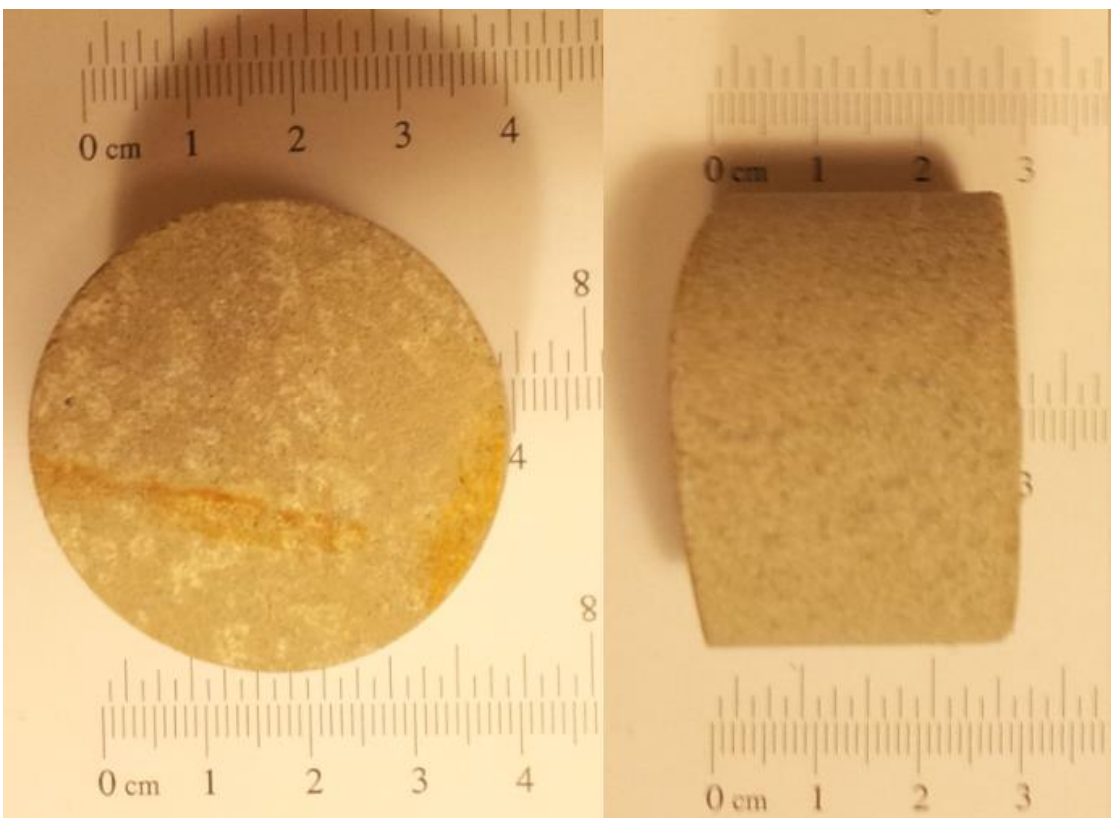

CK3

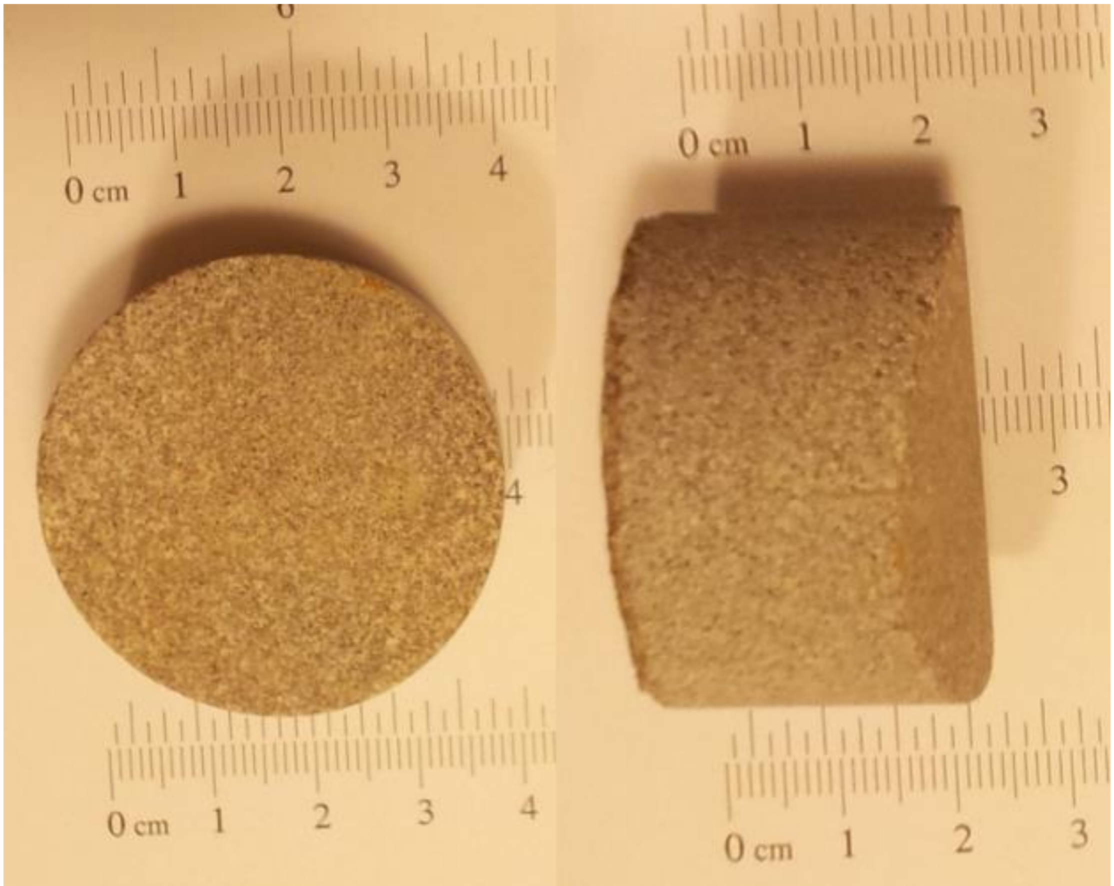

CK4

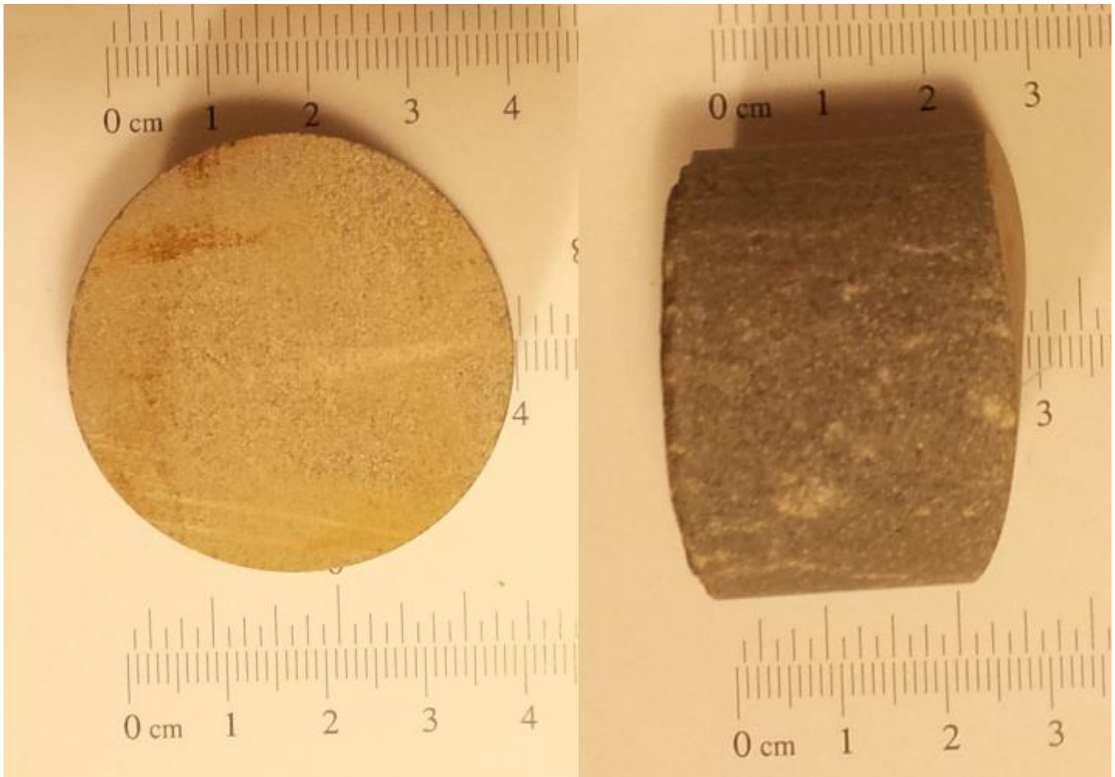

CK5

Historical Core Data Results (NL Oil and Gas Portal)

Hydrostatic Confinement Test						
Depth (m)	**Analysis number**	**Porosity (%)**	**Horiz.perm.(D)**	**Analysis number**	**Porosity (%)**	**Vert.perm.(D)**
3627	5H	9,6	0,00252	5V	9,1	0,00013
3627,25	6H	8,8	0,00038			
3627,5	7H	12,9	0,0328			
3627,75	8H	6,5	0,00039			
3628	9H	9,8	0,00259	9V	10,1	0,0001
3638	49H	13,3	0,323	49V	11,8	0,0503
3638,25	50H	12,5	0,0791			
3638,5	51H	12,4	0,0156			
3638,75	52H	11,7	0,026			
3639	53H	11,5	0,0141	53V	12,2	0,00588
3640	57H	6,8	0,00498	57V	7,1	0,00225
3640,25	58H	6,1	0,00148			
3640,5	59H	9	0,014			
3640,75	60H	13,8	0,0441			
3641	61H	13,3	0,0861	61V	12,9	0,024
3641,25	62H	4	0,00034			
3641,5	63H	7,3	0,00125			
3641,75	64H	9	0,00117			
3642	65H	10,6	0,00867	65V	11	0,00082
3642,25	66H	10,7	0,00637			
3642,5	67H	10,6	0,0046			
3642,75	68H	10,3	0,00298			
3643	69H	10	0,00566	69V	10,5	0,00038
3649	93H	3,7	0,00002	93V	5,2	0,00002
3649,25	94H	5,9	0,00005			
3649,5	95H	4,8	0,00003			
3649,75	96H	5,3	0,00002			
3650	97H	3,7	0,00002	97V	3,1	0,00001
3650,25	98H	3,1	0,00002			
3650,5	99H	2,4	0,00001			
3650,75	100H	2,8	0			
3650,93	101H	5,1	0,00044	101V	3,6	0,00001

CMS-300 TEST						
Depth (m)	**Analysis number**	**Porosity (%)**	**Horiz.perm.(D)**	**Analysis number**	**Porosity (%)**	**Vert.perm.(D)**
3627	5H	9,3	0,00252	5V	8,6	0,00013
3627,25	6H	8,9	0,00038			
3627,5	7H	12,9	0,0328			
3627,75	8H	6,1	0,00039			
3628	9H	9,7	0,00259	9V	9,9	0,0001
3638	49H	13,2	0,323	49V	11,5	0,0503
3638,25	50H	12,7	0,0791			
3638,5	51H	12,6	0,0156			
3638,75	52H	11,5	0,026			
3639	53H	11,6	0,0141	53V	12,1	0,00588
3640	57H	6,8	0,00498	57V	6,9	0,00225
3640,25	58H	6	0,00148			
3640,5	59H	9,3	0,014			
3640,75	60H	13,7	0,0441			
3641	61H	13,3	0,0861	61V	12,7	0,024
3641,25	62H	3,8	0,00034			
3641,5	63H	7,2	0,00125			
3641,75	64H	8,5	0,00117			
3642	65H	10,4	0,00867	65V	11,2	0,00082
3642,25	66H	10,4	0,00637			
3642,5	67H	10,2	0,0046			
3642,75	68H	10,1	0,00298			
3643	69H	10	0,00566	69V	10,9	0,00038
3649	93H	3,3	0,00002	93V	4,6	0,00002
3649,25	94H	5,3	0,00005			
3649,5	95H	4,4	0,00003			
3649,75	96H	4,5	0,00002			
3650	97H	3,4	0,00002	97V	2,5	0,00001
3650,25	98H	2,5	0,00002			
3650,5	99H	2,1	0,00001			
3650,75			0			
3650,93	101H	3,2	0,00044	101V	3,7	0,00001

HOT SHOT ANALYSIS			
Depth (m)	**Analysis number**	**Porosity(%)**	**Horiz.perm.(D)**
3627	5H	8,7	0,00091
3628	9H	10,1	0,0047
3638	49H	13	0,102
3639	53H	11	0,009
3640	57H	6,3	0,0038
3641	61H	13	0,057
3642	65H	10,5	0,0092
3643	69H	10	0,0077
3649	93H	4,1	0,00001
3650	97H	2,9	0,00001
3650,93	101H	2,2	-

Avizo Permeability Output

CK1

ROI (min/max)	Permeability X Axis (D)	Permeability Y Axis (D)	Permeability Z Axis (D)
1804.65 1886.11 565.014 / 2232.15 2312.61 992.514	0,009	0,008	0,009
2299.89 1482.17 629.919 / 2727.39 1909.67 1057.42	0,008	0,007	0,009
1612.85 2650.26 351.433 / 2040.35 3077.76 778.933	0,010	0,010	0,012
3056.9 868.666 1632.06 / 3484.4 1296.17 2059.56	0,007	0,007	0,007
302.865 965.008 1215.41 / 730.365 1392.51 1642.91	0,007	0,007	0,007
2361.08 558.047 1709.08 / 2788.58 985.547 2136.58	0,008	0,008	0,007
427.024 2817.41 1879.88 / 854.524 3244.91 2307.38	0,016	0,016	0,015
86.3579 2206.18 1974.96 / 513.858 2633.68 2402.47	0,015	0,011	0,014
1287.35 1180.55 227.634 / 1714.85 1608.05 655.134	0,012	0,018	0,015
1028.49 2134.79 173.192 / 1455.99 2562.29 600.692	0,015	0,015	0,021
1124.96 1736.09 1386.99 / 1552.46 2163.59 1814.49	0,008	0,009	0,008
1952.39 2326.07 93.7351 / 2379.89 2753.57 521.235	0,029	0,008	0,018
2527.03 1652.89 1018.49 / 2954.53 2080.39 1445.99	0,019	0,011	0,004
665.336 2528.91 1118.96 / 1092.84 2956.41 1546.46	0,007	0,007	0,007
2099.75 1325.94 1784.1 / 2527.25 1753.44 2211.6	0,009	0,009	0,008
926.218 2968.41 772.997 / 1353.72 3395.91 1200.5	0,007	0,007	0,008
2891.38 655.299 495.46 / 3318.88 1082.8 922.96	0,008	0,011	0,012
2722.03 283.847 1288.01 / 3149.53 711.347 1715.51	0,007	0,008	0,008
577.642 331.126 1529.8 / 1005.14 758.626 1957.3	0,008	0,007	0,007
1518.23 1.56855 921.338 / 1945.73 429.069 1348.84	0,009	0,009	0,010

CK2

ROI (min/max)	Permeability X Axis (D)	Permeability Y Axis (D)	Permeability Z Axis (D)
1006.49 2348.65 588.291 / 1433.99 2776.15 1015.79	0,218	0,057	0,146
2101.39 1653.68 799.299 / 2528.89 2081.18 1226.8	0,018	0,085	0,037
2478.38 69.3435 338.343 / 2905.88 496.844 765.843	0,011	0,024	0,014
1732.8 2636.11 1376 / 2160.3 3063.61 1803.5	0,020	0,024	0,012
1628.41 2857.55 865.116 / 2055.91 3285.05 1292.62	0,015	0,028	0,023
1874.85 2271.95 1886.68 / 2302.35 2699.45 2314.18	0,026	0,034	0,040
1527.45 213.809 303.733 / 1954.95 641.309 731.233	0,008	0,021	0,013
94.473 1028.27 66.9938 / 521.973 1455.77 494.494	0,075	0,024	0,033
2179.5 1741.34 1599.57 / 2607 2168.84 2027.07	0,018	0,019	0,033
2955.4 1949.27 1826.97 / 3382.9 2376.77 2254.47	0,013	0,012	0,019
818.735 543.248 1058.06 / 1246.23 970.748 1485.56	0,013	0,011	0,015
2846.86 821.652 632.045 / 3274.36 1249.15 1059.55	0,012	0,013	0,011
721.208 1398.1 1205.54 / 1148.71 1825.6 1633.04	0,023	0,035	0,027
2642.78 1188.24 953.543 / 3070.28 1615.74 1381.04	0,019	0,040	0,023
1374.55 1264.12 1528.95 / 1802.05 1691.62 1956.45	0,082	0,056	0,130
1125.85 659.911 1971.42 / 1553.35 1087.41 2398.92	0,016	0,026	0,011
364.502 316.847 1734.62 / 792.002 744.347 2162.12	0,111	0,220	0,204
180.716 2627.93 453.863 / 608.216 3055.43 881.363	0,045	0,098	0,028
557.816 2112.98 1299.71 / 985.316 2540.48 1727.21	0,095	0,052	0,032
2361.87 2994.87 122.755 / 2789.37 3422.37 550.255	0,015	0,020	0,015

CK3

ROI (min/max)	Permeability X Axis (D)	Permeability Y Axis (D)	Permeability Z Axis (D)
2456.28 592.414 1972.82 / 2883.78 1019.91 2400.32	0,008	0,008	0,008
1508.46 1682.15 1467.79 / 1935.96 2109.65 1895.29	0,009	0,008	0,009
1225.56 62.1226 1068.28 / 1653.06 489.623 1495.78	0,096	0,020	0,025
1946.87 2338.45 1818.2 / 2374.37 2765.95 2245.7	0,017	0,009	0,011
889.403 2487.39 1148.03 / 1316.9 2914.89 1575.53	0,029	0,027	0,036
2586.79 2753.49 1305.93 / 3014.29 3180.99 1733.43	0,078	0,005	0,010
2102.45 3022.75 1598.08 / 2529.95 3450.25 2025.58	0,016	0,018	0,019
291.288 1180.77 420.152 / 718.788 1608.27 847.653	0,015	0,013	0,008
387.952 848.13 116.936 / 815.451 1275.63 544.435	0,013	0,008	0,008
974.72 423.603 1390.35 / 1402.22 851.103 1817.85	0,021	0,011	0,010
117.152 1383.29 1910.23 / 544.652 1810.79 2337.73	0,095	0,033	0,037
1272.29 1790.92 858.017 / 1699.79 2218.42 1285.52	0,007	0,004	0,016
2776.27 2296.2 9.18254 / 3203.77 2723.7 436.682	0,015	0,013	0,017
2262.12 305.707 929.545 / 2689.62 733.207 1357.05	0,020	0,013	0,009
1857.97 2020.39 246.26 / 2285.47 2447.89 673.76	0,013	0,016	0,014
2908.45 1482.06 681.745 / 3335.95 1909.65 1109.24	0,013	0,013	0,009
619.299 625.454 1651.02 / 1046.8 1052.95 2078.52	0,054	0,065	0,045
3068.2 2824.55 772.765 / 3495.7 3252.05 1200.27	0,008	0,008	0,007
752.308 2012.24 521.03 / 1179.81 2439.74 948.53	0,017	0,014	0,019
1662.11 978.804 405.607 / 2089.61 1406.3 833.107	0,010	0,009	0,009

CK4

ROI (min/max)	Permeability X Axis (D)	Permeability Y Axis (D)	Permeability Z Axis (D)
2981.57 39.5136 1001.45 / 3409.07 467.014 1428.97	0,007	0,007	0,007
1929.23 945.935 1954.05 / 2356.73 1373.44 2381.55	0,007	0,007	0,007
2115.88 1373.44 1364.97 / 2543.38 2867.93 1792.47	0,008	0,418	0,008
2658.84 444.554 1746.38 / 3086.34 872.054 2173.88	0,007	0,007	0,007
69.2954 2288.27 570.108 / 496.795 2715.77 997.608	0,007	0,007	0,007
2794.33 2114.04 826.115 / 3221.83 2541.54 1253.61	0,007	0,007	0,007
1720.22 2743.29 204.402 / 2147.72 3170.79 631.902	0,007	0,007	0,008
254.536 2798.98 1474.94 / 682.036 3226.48 1902.44	0,009	0,007	0,007
2548.25 766.428 1147.89 / 2975.75 1193.93 1575.39	0,007	0,007	0,007
565.808 837.461 1616.12 / 993.308 1264.96 2043.62	0,007	0,007	0,007
368.168 1678.4 1851.92 / 795.668 2105.9 2279.42	0,007	0,007	0,007
2199.75 1109.15 1664.27 / 2627.25 1536.65 2091.77	0,007	0,007	0,007
968.608 3071.55 735.289 / 1396.11 3499.05 1162.79	0,007	0,007	0,007
1219.56 2555.1 43.72 / 1647.06 2982.6 471.22	0,007	0,007	0,007
1421.38 1703.73 1046.26 / 1848.88 2131.23 1473.76	0,007	0,007	0,007
1699.73 564.456 376.273 / 2127.23 991.956 803.773	0,007	0,007	0,007
1329.69 2006.08 489.595 / 1757.19 2433.58 917.095	0,007	0,007	0,007
2364.72 276.659 685.48 / 2792.22 704.159 1112.98	0,007	0,007	0,007
653.36 1487.14 247.586 / 1080.86 1914.64 675.086	0,007	0,007	0,007
872.367 1342.2 1247.43 / 1299.87 1769.7 1674.93	0,007	0,007	0,007

CK5

ROI (min/max)	Permeability X Axis (D)	Permeability Y Axis (D)	Permeability Z Axis (D)
2260.81 190.266 116.854 / 2688.31 617.766 544.354	0,007	0,007	0,007
746.213 2669.3 850.62 / 1173.71 3096.8 1278.12	0,007	0,007	0,007
332.013 89.6619 48.6532 / 759.513 517.162 476.153	0,009	0,009	0,009
2387.52 2159.45 1705.61 / 2815.02 2586.95 2133.11	0,009	0,008	0,008
1800.64 2387.28 1459.98 / 2228.14 2814.78 1887.48	0,008	0,008	0,007
120.54 1831.53 267.403 / 548.04 2259.03 694.903	0,007	0,007	0,007
3063.58 1281.03 1371.78 / 3491.08 1708.53 1799.28	0,008	0,048	0,029
1312.99 3014.75 1134.83 / 1740.49 3442.25 1562.33	0,008	0,007	0,008
1481.62 1509.56 1752.16 / 1909.12 1937.06 2179.66	0,007	0,008	0,008
1588.82 1871.35 1235.83 / 2016.32 2298.85 1663.33	0,007	0,007	0,007
2157.34 502.075 1844.48 / 2584.84 929.575 2271.98	0,007	0,007	0,007
2811.39 1101.62 631.599 / 3238.89 1529.12 1059.1	0,007	0,007	0,008
1133.7 1073.47 612.611 / 1561.2 1500.97 1040.11	0,007	0,007	0,007
288.586 2914.2 1123.06 / 716.086 3341.7 1550.56	0,007	0,007	0,007
1880.43 660.221 501.692 / 2307.93 1087.72 929.192	0,007	0,007	0,007
898.301 821.346 2015.87 / 1325.8 1248.85 2443.37	0,007	0,007	0,007
2693.69 1583.29 1018.92 / 3121.19 2010.79 1446.42	0,007	0,007	0,008
1000.02 2245.39 365.19 / 1427.52 2672.89 792.69	0,007	0,007	0,008
2607.74 398.726 782.169 / 3035.24 826.226 1209.67	0,007	0,007	0,007
618.625 2538.21 1578.71 / 1046.12 2965.71 2006.21	0,008	0,008	0,009

Permeameter

For the experimental determination of the permeability of the 5 cores, the PDPK-400™ by Core Laboratories was used. The tests were conducted at the offices of PanTerra Geoconsultants BV.

The apparatus is an instrument that measures permeability based on the calculated pressure decay for the injected nitrogen in either or all of the tanks in the device. The PDPK-400 has a gas permeability measurement range of 0.001 – 30000 mD. Permeabilities are slip corrected (Klinkenberg) and are also corrected for Non-Darcian flow (Forchheimer Factor).

Analog Permeability Measurements

CK1 (D)	CK2 (D)	CK3 (D)	CK4 (D)	CK5 (D)
0,0002	0,0129	0,0028	0,0000	0,0003
0,0002	0,0027	0,0031	0,0000	0,0000
0,0005	0,0057	0,0032	0,0000	0,0000
0,0005	0,0064	0,0033	0,0000	0,0000
0,0005	0,0066	0,0035	0,0000	0,0000
0,0005	0,0102	0,0038	0,0000	0,0000
0,0005	0,0117	0,0039	0,0000	0,0001
0,0005	0,0122	0,0040	0,0000	0,0001
0,0006	0,0127	0,0040	0,0000	0,0001
0,0006	0,0127	0,0040	0,0000	0,0001
0,0006	0,0132	0,0041	0,0000	0,0001
0,0007	0,0132	0,0043	0,0000	0,0001
0,0007	0,0136	0,0044	0,0000	0,0001
0,0008	0,0139	0,0046	0,0000	0,0002
0,0010	0,0139	0,0050	0,0000	0,0002
0,0010	0,0143	0,0050	0,0000	0,0003
0,0010	0,0149	0,0054	0,0001	0,0003
0,0011	0,0156	0,0055	0,0001	0,0003
0,0011	0,0158	0,0057	0,0001	0,0003
0,0013	0,0160	0,0075	0,0001	0,0003
0,0020	0,0171	0,0075	0,0001	0,0004
0,0023	0,0176	0,0149	0,0001	0,0004
0,0031	0,0184	0,0231	0,0005	0,0004
0,0040	0,0189	0,0248	0,0009	0,0004
-	-	0,0587	0,0011	0,0004
-	-	0,0635	0,0017	0,0005

Autoappend MatLAB Code

```
clc;
clear all;
close all;

d=116;

for i=1:d
 s1 = i+3;
 s2 = 2+((i)*3333);
 s3 = 3336+((i)*3333);
  sheet_string = strcat('Sheet',num2str(s1));
 B_Lstring = strcat('B',num2str(s2),':L',num2str(s3));
   tempdata = xlsread('poresck1.xlsx',sheet_string,'B3:L3335');
 xlswrite('poresck1.xlsx',tempdata,'Sheet1',B_Lstring);
end
```